Meteor Radar vertical wind observation biases and mathematical debiasing strategies including a 3DVAR+DIV algorithm

Gunter Stober[1], Alan Liu[2], Alexander Kozlovsky[3], Zishun Qiao[2], Ales Kuchar[4], Christoph Jacobi[4], Chris Meek[5], Diego Janches[6], Guiping Liu[6,7], Masaki Tsutsumi[8,9], Njal Gulbrandsen[10], Satonori Nozawa[11], Mark Lester[12], Evgenia Belova[13], Johan Kero[13], and Nicholas Mitchell[14,15]

[1]Institute of Applied Physics & Oeschger Center for Climate Change Research, Microwave Physics, University of Bern, Bern, Switzerland
[2]Center for Space and Atmospheric Research and Department of Physical Sciences, Embry-Riddle Aeronautical University, Daytona Beach, Florida, USA
[3]Sodankylä Geophysical Observatory, University of Oulu, Finland
[4]Institute for Meteorology, Leipzig University, Leipzig, Germany
[5]University of Saskatchewan, Canada
[6]ITM Physics Laboratory, Mail Code 675, NASA Goddard Space Flight Center, Greenbelt, MD 20771, USA
[7]Space Sciences Laboratory, University of California, Berkeley, CA, USA
[8]National Institute of Polar Research, Tachikawa, Japan
[9]The Graduate University for Advanced Studies (SOKENDAI), Tokyo, Japan
[10]Tromsø Geophysical Observatory, UiT - The Arctic University of Norway, Tromsø, Norway
[11]Division for Ionospheric and Magnetospheric Research Institute for Space-Earth Environment Research, Nagoya university, Japan
[12]University of Leicester, Leicester, UK
[13]Swedish Institute of Space Physics (IRF), Kiruna, Sweden
[14]British Antarctic Survey, UK
[15]University of Bath, Bath, UK

Correspondence: gunter.stober@unibe.ch

Abstract. Meteor radars have become ~~a~~ widely used instruments to study atmospheric dynamics, ~~in particular in~~ particularly in the 70 to 110 km altitude region. These systems have been proven to provide reliable and continuous measurements of horizontal winds in the mesosphere and lower thermosphere. Recently, there have been many attempts to utilize specular/-transverse scatter meteor measurements to estimate vertical winds and vertical wind variability. In this study we investigate potential biases in vertical wind estimation that are intrinsic to the meteor radar observation geometry and scattering mechanism, and introduce a mathematical debiasing process to mitigate them. This process makes use of a spatio-temporal Laplace filter which is based on a generalized Tikhonov regularization. Vertical winds obtained from this retrieval algorithm are compared to UA-ICON model data. This comparison reveals a good agreement in the statistical moments of the vertical velocity distributions. Furthermore, we present the first observational indications of a forward scatter wind bias. It appears to be caused by the scattering center's apparent motion along the meteor trajectory when the meteoric plasma column is drifted by the wind. The hypothesis is tested by a radiant mapping of two meteor showers. Finally, we introduce a new retrieval algorithm providing a physically and mathematically sound solution to derive vertical winds and wind variability from multistatic meteor radar networks such as the Nordic Meteor Radar Cluster (NORDIC) and the Chilean Observation Network De meteOr Radars (CONDOR). The new retrieval is called 3DVAR+DIV and includes additional diagnostic such as the horizontal divergence and relative vorticity to ensure a physically consistent solution for all 3D winds in spatially resolved domains. Based on this new algorithm we obtained vertical velocities in the range of $w = \pm 1 - 2$ m/s for most of the analyzed data during two years of collected data, which is consistent to the values reported from GCMs for this time scale and spatial resolution.

1 Introduction

Vertical wind in the mesosphere/lower thermosphere (MLT) is a key parameter because it is directly related to the vertical transport of momentum, energy, and constituents that drive the global meridional circulation, which is related to almost all dynamical processes in the global atmosphere (e.g. Smith et al., 2010; Qian et al., 2017; Guo and Liu, 2021). However, measuring vertical wind is one of the most challenging remote sensing tasks. The main reason is that the magnitude of long-term mean vertical wind is very small, often beyond the accuracy achievable with any instruments, while instantaneous, or short-duration vertical wind can be large but requires measurements at high temporal and spatial resolutions. Models predict vertical motions on seasonal time scales, at their typical horizontal grid resolution of about 100-200 km, on the order of 0.1 to a few cm/s, e.g., in the Kuehlungsborn Mechanistic Circulation Model (KMCM) and the Whole Atmosphere Community Circulation Model (WACCM) ~~(Becker, 2012; Smith, 2012)~~(Holton, 1983; Becker, 2012; Smith, 2012). At higher solutions, the models are able to resolve smaller scale gravity waves and produce larger vertical winds. In Liu et al. (2014), the high resolution WACCM at 0.25° horizontal resolution produced vertical wind of 7-8 m/s in the lower thermosphere above a tropical cyclone. In a more recent study using the High-Altitude Mechanistic Circulation Model (HIAMCM) with a horizontal resolution of about 55 km, vertical wind ~~velocities~~ speeds up to 3 m/s are reported at an altitude of about 80 km (Becker and Vadas, 2018). High resolution observations such as those made with a sodium lidar also measured vertical wind, showing that tidal perturbation in vertical wind can reach tens of cm/s (Yuan et al., 2014). On the other hand, models and observations also indicate that the horizontal wind magnitudes at the MLT are typically one to two orders of magnitude larger (Miyoshi et al., 2017; McCormack et al., 2017; Borchert et al., 2019; Hocking et al., 1997; Batista et al., 2004; Hoffmann et al., 2007; Jacobi et al., 2009; Wilhelm et al., 2019; Stober et al., 2019). This large difference in the magnitudes between the horizontal and vertical wind component poses an additional challenge to the observational methods, measurement analysis, and parameter estimation of vertical wind due to the requirement of clear separation between vertical and horizontal components.

During the past decades there have been many attempts to measure vertical wind velocities using High-Power-Large-Aperture radars such as EISCAT (Fritts et al., 1990; Hoppe and Fritts, 1995a, b). These EISCAT observations, with a temporal resolution of seconds, showed vertical velocities up to ±10 m/s in the MLT and indicated the presence of a systematic vertical wind bias. Although the EISCAT campaign was conducted during the summer months using polar mesospheric summer echoes as tracers, the mean vertical velocities showed a downward motion, which is contrary to what models suggest for this time of the year. The systematic deviation was attributed to gravity wave motions interacting with the tracer. More recently, Gudadze et al. (2019) presented vertical wind observations over two full summer seasons with the Middle Atmosphere Alomar Radar System (Latteck et al., 2012) and confirmed the presence of a mean vertical wind bias and examined potential error sources in the data analysis. Gudadze et al. (2019) concluded that the mean wind bias of a net downward motion in the center of the PMSE layer can be explained by the sedimentation speed of the ice particles. Removing this sedimentation speed resulted in a effectively zero wind speed or a very small upward motion in the order of a few cm/s.

In addition to these direct vertical wind observations using line of sight velocities, there are also indirect methods. For example, Vincent et al. (2019) derived mean vertical wind velocities by exploiting cross-calibrated MF-radar winds, and considering the horizontal divergence between the pole and the latitude of the observations. This study reported the summer time mean vertical motions of a few cm/s using measurements between 1994-2018. The magnitude and sign of these vertical winds were in agreement to the values obtained by GCMs. Radiometers also offer an indirect methodology by measuring trace gases such as water vapor or ozone (Schranz et al., 2019). Straub et al. (2012) estimated the vertical motion of air parcels from water vapor observation during Sudden Stratospheric Warmings and obtained vertical velocities of a few mm/s at 70-80 km altitude. Such trace gas observations are suitable for inferring vertical motions, which are too small to be observed by direct line of sight measurements , which and often do not reach a sufficient sensitivity to detect such small velocities within the instrument error bounds.

Meteor radar observations have been widely used to measure horizontal winds and atmospheric waves (Hocking et al., 2001; Holdsworth (Hocking and Thayaparan, 1997; Hocking et al., 2001; Holdsworth et al., 2004; Jacobi et al., 2007; Fritts et al., 2010b; Meek et al., 2013; . Horizontal winds are often derived from meteor radar observations assuming a zero vertical wind, which apparently results in reliable wind speeds compared to meteorological analysis data such as the Navy Global Environment Model - High Altitude (NAVGEM-HA) (Eckermann et al., 2018; McCormack et al., 2017). However, there were also some attempts to fit vertical winds to the observations (e.g., Egito et al., 2016; Chau et al., 2017; Conte et al., 2021; Chau et al., 2021, and references therein), which resulted in spurious and apparently very fast vertical motions of up to 20 m/s over several hours or up to 10 m/s over several days. Considering the large observational volumes of about 350 km in diameter in the mesosphere, these values are unlikely to be representative of typical atmospheric motions. For such high vertical velocities to be sustained over hours or even days would require large energy reservoirs, and would be accompanied by strong adiabatic cooling (heating) for upwelling (downwelling) motions, which so far has not been confirmed by co-located satellite observations or other temperature measurements.

In this study, we investigate potential biases of meteor radar wind measurements and present mathematical approaches to minimize their impact on the estimated parameters with a particular emphasis on vertical winds. We present observations from monostatic meteor radars as well as from multistatic meteor radar networks such as the Nordic Meteor Radar Cluster and CONDOR (Chilean Observation Network De meteOr Radars) (Stober et al., 2021a). The vertical wind bias is discussed considering the trail physics and scattering geometry (Poulter and Baggaley, 1977; Jones and Jones, 1990; Stober, G. et al., 2021). Furthermore, fragmentation of meteoroids plays a role in the trail formation and, thus, could lead to biases due to the more complicated trail physics (Subasinghe et al., 2016; Vida et al., 2021). However, as it is not feasible to analyze all these physical processes for each individual meteor, and it is nearly impossible to correct ~~these effects for each meteor~~all effects with most currently available instruments. Thus, we propose mathematical approaches to reduce potential biases by introducing mathematical parameterizations of these effects ~~.~~ to obtain statistical more sound solutions and to avoid artificially large vertical velocities. Furthermore, we introduce a new 3DVAR+DIV retrieval by combining the the radial velocity and continuity equation, which presents already a transition from purely observation driven parameter estimation to more physics and model based data analysis well-known from meteorological reanalysis data sets (Gelaro et al., 2017). Such more complicated physics based models might be even time dependent and, thus, open the gates to generate observations driven forecasts or to implement 4DVAR or 4DVAR-hybrid approaches in the future.

2 Meteor Radar observations and sampling biases

Meteor radars have been widely used to investigate atmospheric dynamics as well as meteor astronomy over the past decades (Hocking et al., 1997, 2001; Portnyagin et al., 2004; Brown et al., 2008a; Fritts et al., 2010a; McCormack et al., 2017; Stober et al., 2012, 2021a; Janches et al., 2015). The systems have been proven to be reliable and suitable for long-term continuous and automated observations of MLT winds and tides (Larsen et al., 2003; Franke et al., 2005; Jacobi et al., 2007; Wilhelm et al., 2019; Stober et al., 2021b; de Araújo et al., 2020). In this study, we use data from two multistatic meteor radar networks, which are ~~the Nordic Meteor Radar Cluster (NORDIC)~~ NORDIC and CONDOR, as well as the single station meteor radars at Collm (COL) and Tierra del Fuego (TDF). The Nordic Meteor Radar Cluster consists of 5 monostatic systems at Svalbard (SVA), Tromsø (TRO), Alta (ALT), Kiruna (KIR) and Sodankylä (SOD). CONDOR makes use of the monostatic radar at the Andes Lidar Observatory (ALO), and two passive receiver systems at the Southern Cross Observatory (SCO) and at Las Campanas Observatory (LCO). Table 1 contains an overview of the geographic location of all systems and the corresponding experiment settings.

MLT winds are obtained from meteor radar observations by applying a so-called all-sky fit (Hocking et al., 2001; Holdsworth et al., 2004), which minimizes the residuals of the projection of all ~~measured radial ,~~ radial or line-of-sight, velocities onto a mean 3D wind within an altitude-time bin in a least-squares sense. The radial ~~wind~~ velocity equation is often written as;

$$v_r = u\cos(\phi)\sin(\theta) + v\sin(\phi)\sin(\theta) + w\cos(\theta) \quad . \tag{1}$$

Here v_r is the line of sight velocity, u, v and w represent the 3D wind velocities in the zonal, meridional and vertical direction, θ denotes the ~~off-zenith angle~~ zenith angle (also often referred to zenith angle) and ϕ is the azimuth angle counterclockwise from East. In general, the vertical wind is assumed to be negligible (w=0 m/s), which simplifies the equation to the horizontal wind components. Obviously, this assumption is justified considering the good agreement of the obtained horizontal winds when compared to meteorological analysis data (McCormack et al., 2017; Stober et al., 2019; Liu et al., 2020) and the large observation volume of about 350 km in diameter as well as the typical temporal resolution of one hour.

Although it appears to be legitimate to make the simplification and to remove the vertical wind from the radial ~~wind~~ velocity

Table 1. Technical parameters of the Nordic Meteor Radar Cluster (SOD, KIR, ALT, TRO), CONDOR (ALO), Tierra Del Fuego (TDF) and Collm (COL).

	TRO	ALT	SOD	KIR	TDF	ALO	COL
Freq. (MHz)	30.25	31	36.9	32.50	32.55	35.1	36.2
Peak Power (kW)	7.5	8	7.5/15	6	64	48	15
PRF (Hz)	500	430	2144	2144	2144/625	430	2144/625
coherent integration	1	1	4	4	4/1	1	4/1
pulse code	4-bit complementary	4-bit complementary	mono	mono	7-bit Barker	4-bit complementary	7-bit Barker
sampling (km)	1.8	1.8	2	2	1.5	1.8	1.5
latitude	69.59°N	70.0°N	67.4°N	67.9°N	53.7°S	30.3°S	51.3°N
longitude	19.2°E	23.3°E	26.6 °E	21.1°E	67.7°W	70.7°W	13.0°E

equation, there is a need for a mathematical justification. Therefore, we investigate the bias that is intrinsic to meteor-radar wind estimates by implementing different data analysis pipelines to the COL and TDF meteor radar using three months of data from January to March 2020. The first data analysis applies a least squares fit using all three wind components, a non-linear error propagation and World Geodetic System 1984 (WGS84~~geometry~~) geometry (National Imagery and Mapping Agency, 2000). The wind components are estimated by a singular value decomposition as solver (Press et al., 1992). The second data analysis leverages the same observations, but all radial velocities were replaced by synthetic data sustaining the spatial and temporal sampling of the original measurements and their corresponding statistical errors. The synthetic wind field is composed of an altitude dependent mean wind, planetary waves, and tides plus some gravity waves. However, the vertical wind component was set to zero for all waves and the mean wind at all altitudes and times.

Figure 1 shows four histograms of hourly fitted vertical winds applying the classical least squares approach solving the radial wind equation. The left histograms present the vertical winds from our 'naive' data analysis. The right panels ~~visualizes the radial~~ visualize the vertical velocity distribution for the synthetic data where we put a zero vertical wind component for all waves. The histograms indicate rather large 'apparent' vertical velocities. In particular, the analyzed synthetic data demonstrates that there are substantial biases considering the width of distribution forming tails beyond a few m/s. However, the synthetic data also exhibits a reduced standard deviation compared to the 'naive' least squares solutions suggesting that there is at least some sensitivity left to 'infer' a residual vertical wind from the observations. The difference between TDF and COL for the synthetic data is only related to the observational statistics. TDF has about twice the number of detections during this part of the season.

There are many reasons for the intrinsic bias in the meteor radar vertical winds. Some of them are almost impossible to address due to the lack of information provided by the current generation of meteor radars. For instance, the question arises how

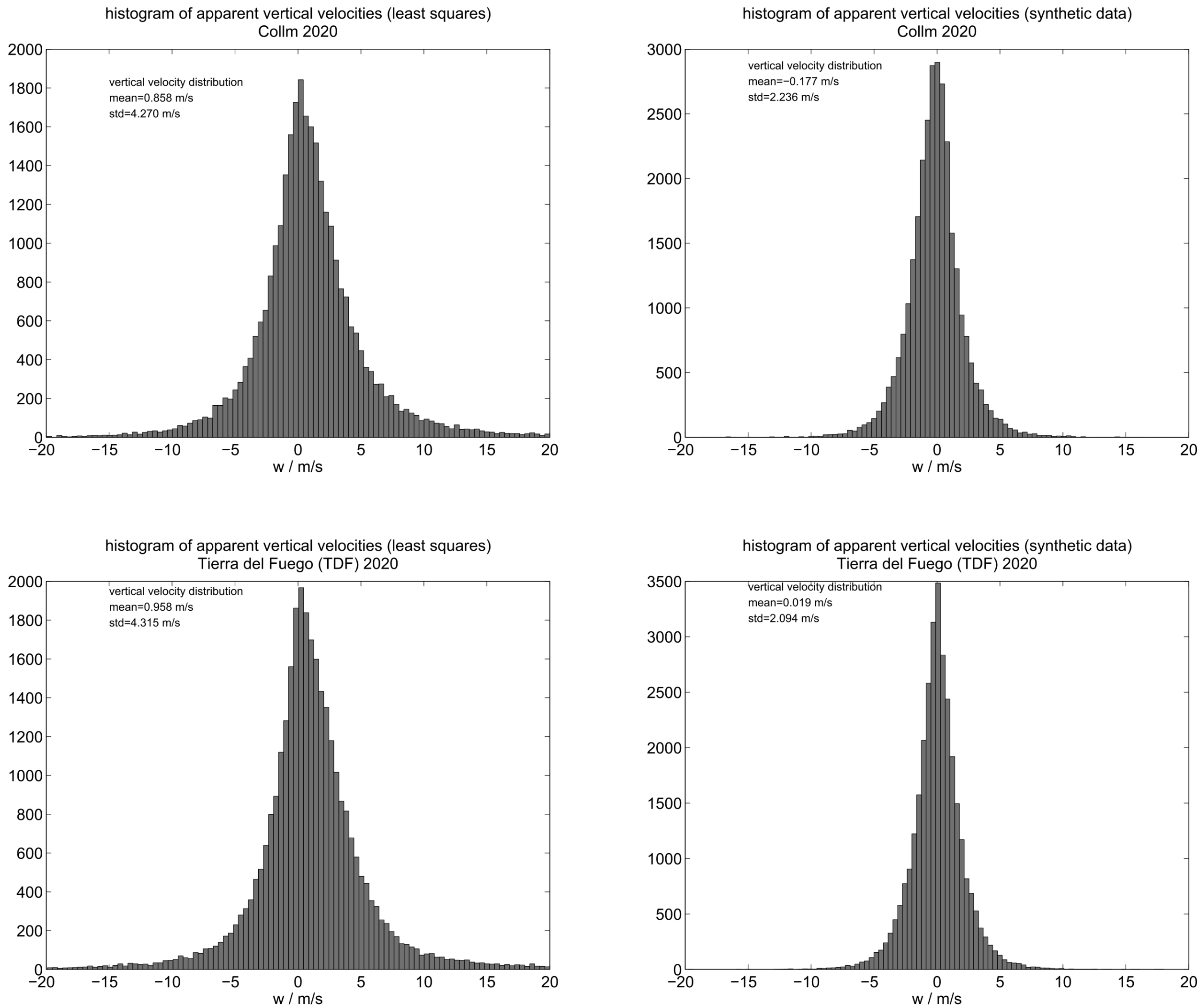

Figure 1. Histograms of the residual bias vertical velocities derived from the COL and the TDF meteor radar using observations from January to March 2020. The left histograms shows the results of the hourly residual bias vertical velocities applying a least squares fit. The right panels show the resulting vertical velocities applying the same algorithm using the COL and TDF detections (volume sampling), but with synthetic data based on mean winds, planetary waves, and tides and a zero vertical velocity.

fragmentation affects the radial velocity measurement and the interferometric solution. Trajectory information to correct for geometric offsets due to the specular/transverse scattering geometry is often not available. Recent studies of high resolution optical observations indicated that almost 90% of the observed meteors exhibit signs of fragmentation (Subasinghe et al., 2016; Vida et al., 2021). There is also the question whether strong wind shear or turbulence induce an apparent motion of the scattering center along the trail axis. Most meteor radars lack the capabilities to investigate and quantify these effects in detail. Only very few systems provide multistatic trajectory measurements, which are required to remove most of the wind shear and geometric effects (Webster et al., 2004; Jones et al., 2005; Brown et al., 2008b; Fritts et al., 2010b; Panka et al., 2021).
Another important aspect in the data analysis is related to the interferometric uncertainties of the angle of arrival (AoA). The receiver antenna array is typically arranged as an asymmetric cross with antenna spacing of 1λ and 1.5 λ or 2λ and 2.5 λ or other combinations. Although such an array is often called Jones array (Jones et al., 1998), it was developed and applied also in other disciplines (Rhodes et al., 1994). Interferometric solutions obtained from such arrays show errors of about 0.5-1°. These errors are included in the retrieval through a Gaussian error propagation in all quantities. Therefore, we adapted the procedure outlined in Gudadze et al. (2019). A more detailed discussion of the positions errors and the reliability of the forward scatter meteor radar observations can be found in Hocking (2018); Zhong et al. (2021). Furthermore, small angular errors also result in altitude uncertainties. These measurement errors are mitigated by estimating the vertical shear from the spatio-temporal Laplace filter.
However, our synthetic data analysis points out that there are also mathematical and geometrical reasons causing an intrinsic bias in the vertical velocities due to the spatial and temporal sampling. The synthetic data does not suffer from any disturbances related to the meteor trail physics. All radial velocities and their interferometric locations in the WGS84 coordinates are exactly determined and ~~, thus,~~ only numerical and sampling aspects due to the time-altitude binning contribute to the standard ~~variation~~ deviation of the distribution shown in Figure 1 (right panel). We also point out that the synthetic data uses all statistical covariances and measurement errors as the real observations to ensure a comparability on fair grounds. Furthermore, the radial wind equation is linear in all three wind components, which results in a weighted measurement response of the $\sin$ and $\cos$-terms for the ~~off-zenith~~ zenith angles. Typical meteor radars detect most of the meteors at ~~off-zenith~~ zenith angles between 55-65° corresponding to a scale factor of 1.2 to 1.3 in the geometric measurement response between the horizontal components and the vertical wind. In addition, it is worth ~~to consider~~ considering that the magnitude of the horizontal wind velocity is often more than a factor of 10 larger compared to the vertical wind magnitude. The consequence of these scaling-terms is also reflected in the statistical uncertainties of the fitted wind coefficients, which range between 2-12 m/s or occasionally more than 15 m/s for each coefficient. These statistical uncertainties are reasonable for horizontal winds, which very often exceed 20-40 m/s as mean wind speed, but are too large to retrieve physical and statistically sound solutions for the vertical velocities.

3 Bias related to scattering geometry

Transverse scatter or specular meteor radars are highly sensitive to the observation geometry. Full wave scattering simulations point out that there is a strong polarization dependence between the trail alignment and the polarization of the incident radio wave (Poulter and Baggaley, 1977; Stober, G. et al., 2021). The concept of meteor radar wind observation is based on the assumption that most of the backscattered radio energy originates from the specular point, which is assumed to be a well-defined location along an infinitely long ambipolar diffusing plasma column. However, the scattering point describes the motion of the scattering center rather than a well-defined location of the meteor trail. Thus, depending on the observing geometry, the measured Bragg vector denotes the motion of this scattering center, which is composed of the trail motion and apparent changes caused by the scattering geometry. These changes in the geometry are related to horizontal or vertical winds and wind shears, and electron line density variations caused by turbulence, fragmentation (Subasinghe et al., 2016; Vida et al., 2021), or differential ablation (Vondrak et al., 2008).

Figure 2 schematically illustrates how these apparent motions of the specular point relate to purely horizontal or vertical movements of the trail. The letter 'A' describes the position of the specular point along the trail after the meteoroid passed the t_0-point (closest distance to the transmitter, see also ~~McKinley (1961); Mazur et al. (2020)~~McKinley (1961); Hocking (2000); Mazur et al. (2020)) and 'B' labels the location of this specular point if it stays 'glued' to the trail, while the meteoric plasma column is drifted by the neutral wind. 'C' labels the position of the scattering center considering the trail motion, but sustaining the geometry regarding the transmitter and receiver location (TX/RX). Although the concept of the specular point as a reflection center is already a substantial simplification of the scattering process, the scheme visualizes the basic geometric problem. A more realistic approach considers that the scattering actually occurs from an extended section of the meteoric plasma trail along the meteor flight path containing several Fresnel zones around the specular point.

The ~~later~~ latter point is of particular concern for multistatic or forward scatter meteor radar observations. Due to the ~~more slant incident radiowave the~~ larger smaller angle between the incident radiowave and the meteoric plasma column, the scattering section along the trail is much longer. Already Stober and Chau (2015) demonstrated that the forward scatter angle corresponds to a frequency shift to lower frequencies and, thus, to even larger Fresnel zones. Hence, changes of the electron line density within the scattering section along the trail act as an additional weighting and lead to even more pronounced apparent motions of the specular point, which can slide along the meteor trajectory. This sliding can be caused by changes of scattering geometry due to winds and wind shears or by modifications of the electron line density that are associated with fragmentation and differential ablation.

We evaluate the above described hypothesis by performing a normal wind analysis using all three data sets provided by the CONDOR network in Chile. The network is unique in the sense that it combines ~~monostatic~~ a monostatic meteor radar and forward scatter passive receivers in a fairly compact geographic region. Figure 3 shows a comparison of the zonal (left column) and meridional (right column) winds using only the northernmost site at LCO, the standard meteor radar at ALO and the passive receiver at SCO. A geographic map of all three sites can be found in Stober et al. (2021a). The observation volumes are basically overlapping to about 60%, and, thus, it is reasonable to expect that a climatological comparison should result in an almost identical mean wind behavior. However, zonal winds exhibit large differences especially during May to September and at altitudes below 85 km. Above 85 km, discrepancies appear to be much smaller. The excess of the zonal wind magnitude between the monostatic (ALO) and the forward scatter stations is about a factor of 2 around 80 km and below. There is no geophysical reason why in such a narrow latitudinal band the zonal wind should show such significant changes. We reproduced

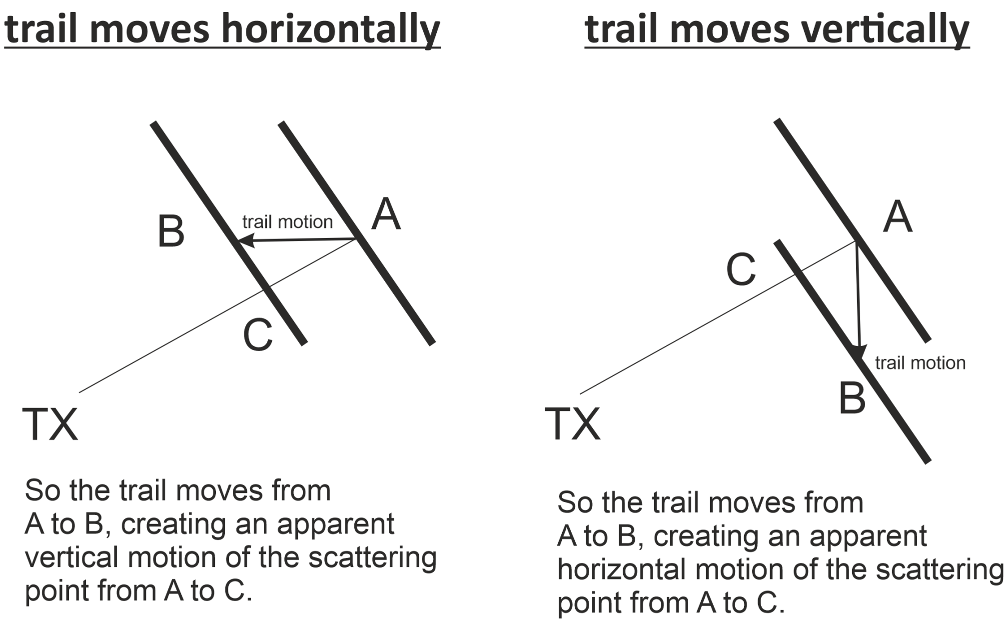

Figure 2. Idealized schemes of the specular scattering geometry indicating the apparent motion of the specular point or scattering center along the trail due to the drift of the meteor plasma column by neutral winds. The length of the meteoric trails is several kilometer, whereas the apparent motions of the scattering center is in the order of meteor. The label 'A' shows the position of the specular point at the first detection, 'B' denotes the location of the scattering center assuming it stays glued to the same mid-point of the trail and 'C' shows the position of the reflection point sustaining the transmitter and receiver geometry.

these results with a commercial software (Holdsworth et al., 2004) to rule out any issues caused by the retrieval algorithm that is described in detail in section 4. It is evident from Figure 3 that the zonal wind appears to be significantly stronger above the passive forward scatter receivers. Meridional winds seem to be much less affected, although there are substantial difference between the northernmost and southernmost location, which are only separated by 3° in latitude. Our preliminary analysis thus already reveals that there is a considerable ~~and~~ altitude dependent difference in the wind magnitude between monostatic and passive receiver systems.

Finally, we investigate whether the magnitude difference manifests also in the Bragg vector pointing direction between the forward scatter receivers at SCO and LCO relative to the monostatic radar at ALO. In Figure 2 we hypothesized that the Bragg vector pointing direction is not affected by the trail motion due to the wind, which is described by a parallel translation, and, thus the Bragg vector pointing is supposed to remain perpendicular to the meteor trajectory for underdense meteors, whereas the length of the Bragg vector is a measure of the total path of the scattering center over successive radar pulses, which includes the motion of the trail due to the neutral wind plus an apparent sliding of the scattering center (specular point) along the trail. We computed the source radiant of two well-known and long lasting (several degrees in solar longitude) meteor showers applying a modified single station radiant mapping algorithm (Jones and Jones, 2006). The meteor source radiant maps for SCO, LCO and ALO were obtained by implementing a revised version of the algorithm applied in Stober et al. (2013). The new

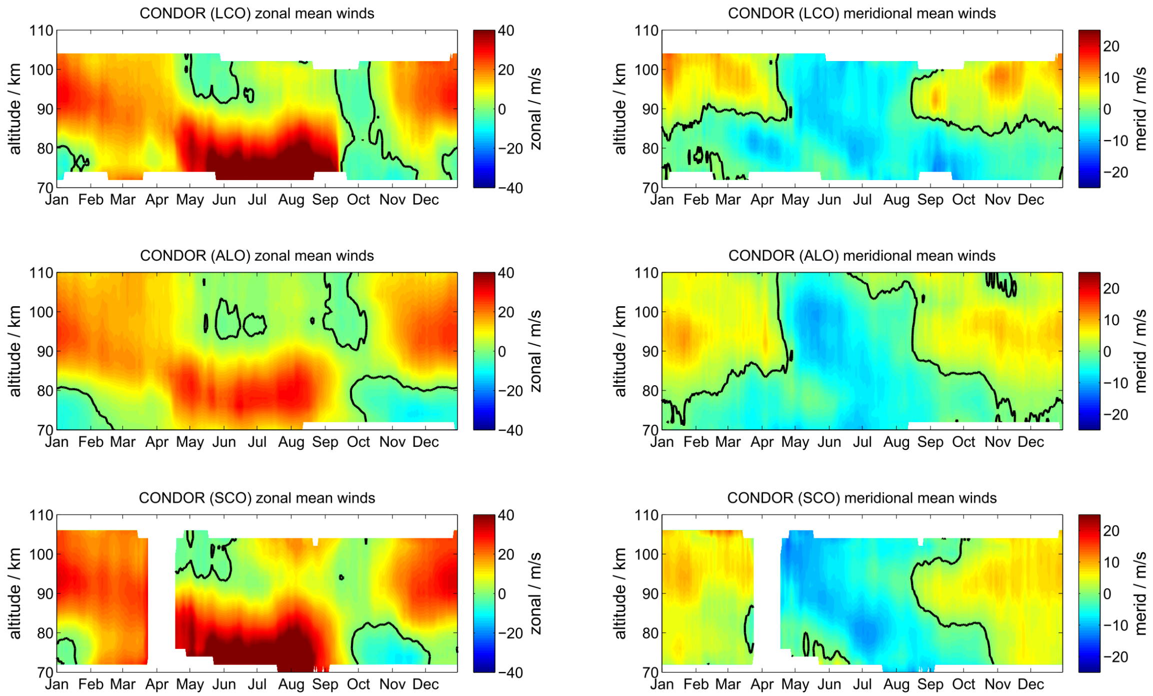

Figure 3. Comparison of zonal and meridional winds as composite from 2012 to 2021 for the forward scatter receiver stations LCO and SCO and the monostatic radar in ALO. The left column shows the zonal wind component and the panels on the right the meridional wind. The panels are sorted according to their geographic latitude with the northernmost sampling volume at LCO on top, the ALO in the center and the southernmost station SCO in the lowest row.

generalized radiant mapping is based on the WGS84 geometry for each individual meteor. There have been already several meteor shower catalogues published in the literature covering the northern and southern hemispheres (Brown et al., 2010; Janches et al., 2013; Pokorny et al., 2017) and, hence, it was easy to pick some of the established meteor showers for the solar longitudes of concern. Figure 4 shows six radiant activity maps for LCO, SCO and ALO. At the beginning of May all three sites exhibit an increased activity at the source radiant of the eta-Aquariids (ETA), which are visible at right ascension $\alpha = 337°$ and declination $\delta = -0.9°$. This meteor shower is active between solar longitudes of λ_{sol}=30-60°, corresponding to the end of April until May (Brown et al., 2010; Janches et al., 2013). The second shower that we found was the Daytime zeta Perseids (ZPE), which is visible at right ascension $\alpha = 56.6°$ and declination $\delta = 23.2°$. Daytime zeta Perseids are active between solar longitudes λ_{sol}=56-90°, corresponding to the end of May until June (Brown et al., 2010; Schult et al., 2018). The right ascension and declination coordinates are provided for the days around the maximum meteor shower activity. These radiant activity maps indicate no systematic differences that explain the differences in the Bragg vector magnitudes between the forward scatter stations at SCO and LCO and the monostatic radar at ALO. More detailed position information for both meteor showers is presented in Appendix B1. Thus, the Bragg vectors are correctly determined for all stations and reflect no substantial deviation of the source radiant for these two meteor showers. In particular, the Daytime zeta Perseids have a

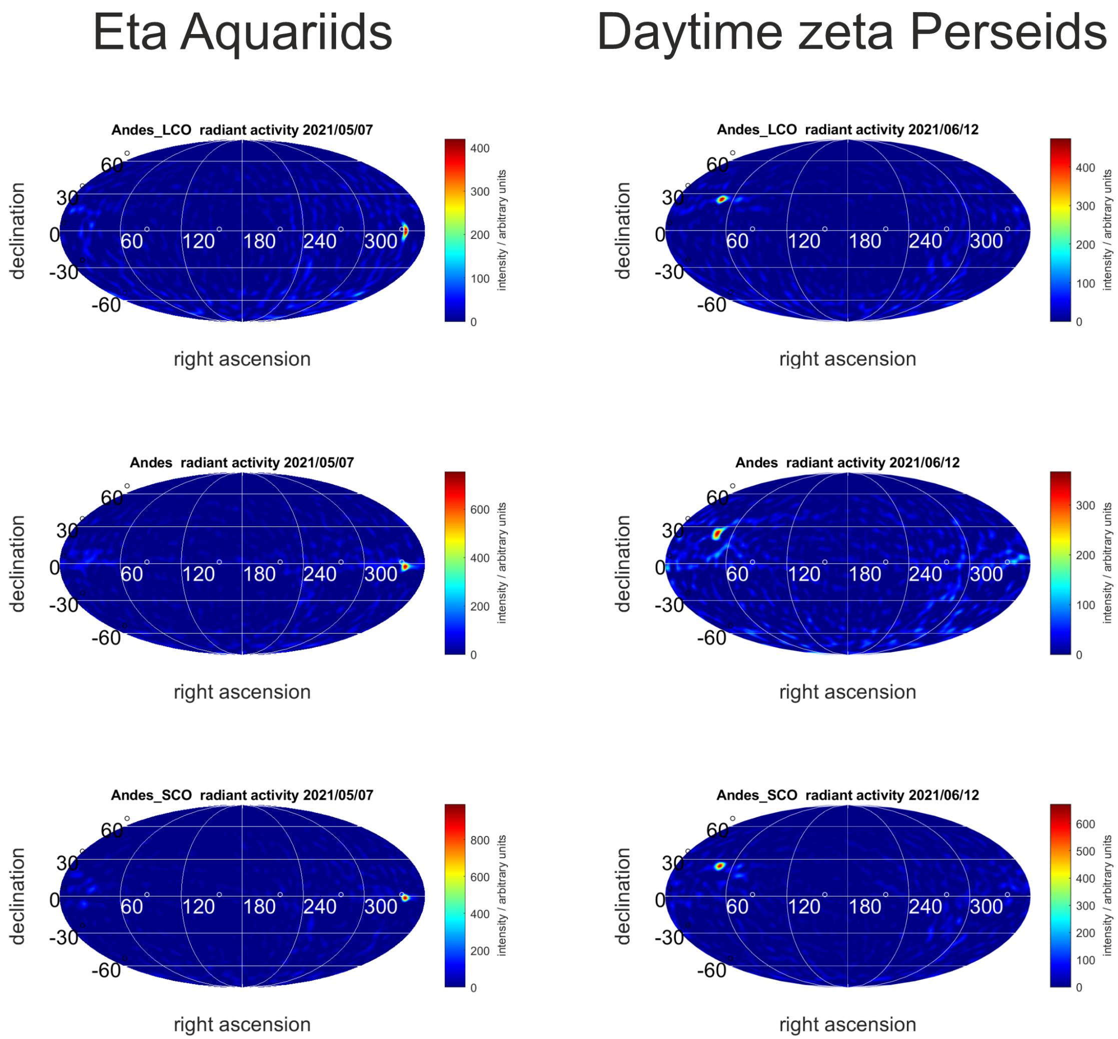

Figure 4. Meteor radiant activity maps derived from CONDOR for LCO, ALO(Andes) and SCO (the top, middle and bottom row, respectively) . The left column shows the source radiant activity for the η-Aquariids and the right panels present the Daytime zeta Perseids. The meteor showers are identified from the catalogues presented in Brown et al. (2010); Janches et al. (2013).

geocentric velocity of $v_g = 28 - 32$ km/s and, hence, can penetrate deep into the atmosphere and reach the altitudes where we already see significant differences in the wind magnitudes. In summary, we were not able to identify a similar deviation in the source radiant mapping of two major meteor showers between the forward scatter receiver stations and the monostatic radar that corresponds to or explains the magnitude offset that is evident in the zonal winds.

4 Mathematical debiasing strategies

After we introduced the intrinsic bias of the vertical wind estimates in meteor radar observations, we are going to briefly discuss mathematical debiasing strategies. The most straightforward method is to implement a Tikhonov regularization in the least squares fitting (Wilhelm et al., 2017; Stober et al., 2017). However, this approach leads to a brute force norm reduction and depends on an empirically determined Tikhonov matrix and Lagrange multiplier;

$$||Ax - b||^2 + \lambda||\Gamma x||^2 \quad . \tag{2}$$

Here A is the Jacobian matrix of the problem, x is our state vector, b are the observations, Γ denotes the Tikhonov matrix, λ describes the Lagrange multiplier (here and further on $\lambda = 1$), and the superscripts on the vertical lines denote the Euclidean norm. It is now possible to construct a Tikhonov matrix in such a way that $\lim_{\Gamma_w \to \infty} \Gamma x \to \infty$, which results in w=0 m/s for all solutions and, thus, is equivalent to the assumption of a negligible wind. The infinite growth of the right hand side enforces a norm reduction for the vertical wind and, hence, the vertical wind solution converges to zero. However, it is also possible to insert a solution of $\Gamma_w \in [0, \infty)$, which in consequence leads to a strong damping of the artifically large vertical velocities. The most straightforward approach is to use the ~~unit~~ identity matrix as Tikhonov regularization, which is known as damped least square but does not satisfactory remove the vertical wind bias.

Although a Tikhonov regularization is suitable to ~~enforce small~~ suppress artificially large vertical velocities, we are going to outline an even more complex approach to solve for the vertical wind. To this end, we modify the Tikhonov regularization to a filter function, which is also known as generalized Tikhonov regularization. Due to the implemented spatio-temporal Laplace filter in the meteor radar retrievals, it is straightforward to estimate a predictor for the state vector x_a for each time-altitude bin (Stober et al., 2019, 2021a). Furthermore, we can insert constraints to the error covariance for the state vector accounting for the above described scaling effects between the horizontal and vertical wind components. Thus, we now solve the problem using the form;

$$||Ax - b||_P^2 + \lambda||\hat{\Gamma}(x - x_a)||_Q^2 \quad . \tag{3}$$

Here, P denotes the inverse covariance matrix of b, and Q is the inverse covariance of x including a scaling term for the vertical wind component to remove the bias and again to remove the artificially large vertical velocities. The advantage of the new norm reduction is that for small differences $x - x_a$ and reasonable covariance errors the solution is identical to the least squares fit as the right hand term of Eq. 3 basically vanishes. By construction the right hand term permits a certain part of the solution to pass through the spatio-temporal Laplace filter depending on its covariance. The larger the statistical uncertainties, the stronger and more important ~~becomes the right hand term~~ the right-hand term becomes, which often results in smaller vertical velocities.

Furthermore, the spatio-temporal Laplace filter is also beneficial for the horizontal wind components to compensate and reduce effects caused by the random and irregular spatial and temporal occurrence of meteors within the sampling (observation) volume of the radar. Sometimes, small or even tiny measurement errors in the location of a meteor may induce large projection errors in the final solution of the retrieved wind components, which is minimized and mitigated when applying the spatio-temporal filter.

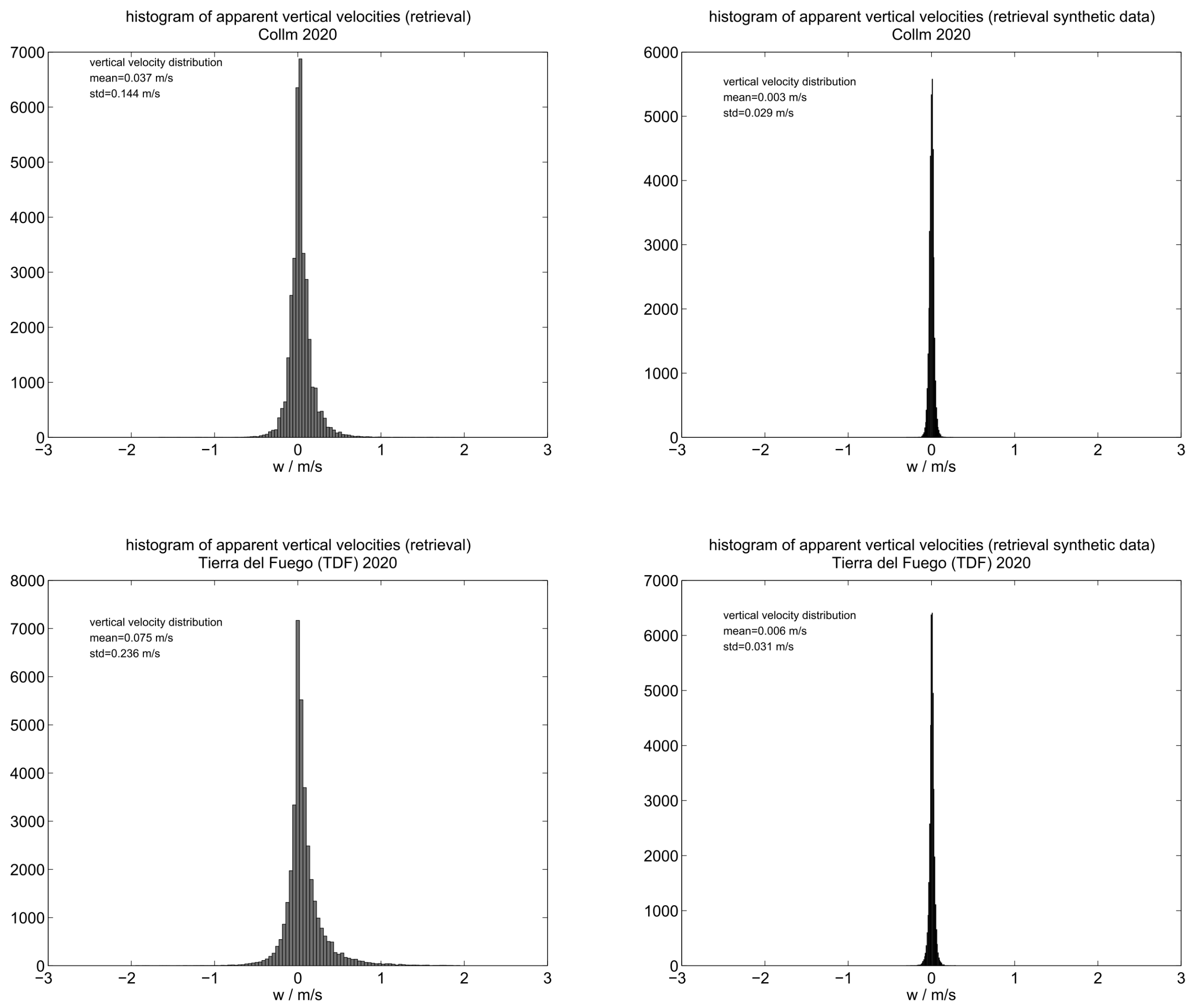

Figure 5. The same as Figure ~~2~~1, but the hourly vertical winds are obtained by applying the retrieval algorithm including the spatio-temporal Laplace algorithm. The x-axis scale or w-axis scale was reduced to show the remaining variability.

Figure 5 shows the vertical velocity histograms based on the retrieval algorithm applying the spatio-temporal Laplace filter and the empirical bias correction based on the scale analysis. The left panel shows the inferred vertical velocities based on the original COL and TDF observations. The ~~histogram~~ histograms in the right ~~panel is~~ panels are obtained when the synthetic data set, with all vertical wind values being zero, is analyzed with the retrieval algorithm. The remaining width of the distribution is caused by the sampling window in time and space (vertical bin size) and ~~the~~ other atmospheric waves. However, ~~already~~ this simple de-biasing approach, where we just consider the scale analysis described above, substantially reduced the offset that was inherent when only a 'standard' least squares wind fit (Press et al., 1992) was applied (Figure 1 right panel). Although,

~~however,~~ generalized Tikhonov regularizations or filtering functions such as the spatio-temporal Laplace filter can help to reduce the intrinsic bias in the meteor radar wind analysis to determine vertical winds by comparing idealized synthetic data, we are still not able to prove the reliability of the derived vertical winds beyond their statistical properties due to a missing ground 'truth'.

5 Statistical comparison to the non-hydrostatic UA-ICON model

A direct comparison of the retrieved vertical winds to other observations is not feasible due to the lack of such measurements. Therefore, we prepared a statistical comparison to a recently developed state of the art non-hydrostatic General Circulation Model (GCM). The Upper Atmosphere ICOsahedral Non-hydrostatic (UA-ICON, Borchert et al., 2019) extends the vertical coverage of the ICON numerical weather prediction model from 80 km to about 150 km altitude. A detailed description of the upper atmosphere physics is given in Borchert et al. (2019). The upper atmosphere version leverages the numerical weather prediction physics packages (Zängl et al., 2015; Giorgetta et al., 2018; Crueger et al., 2018). Here we made use of a 21 year free running climate simulation without any nudging and parameterized gravity waves on a so-called R2B4 grid with a horizontal resolution of 160 km (Borchert et al., 2019; Giorgetta et al., 2018). Above 120 km altitude the model applies Rayleigh damping on the vertical winds. The benefit of the UA-ICON model for such a comparison is that vertical winds are available on a geometric vertical coordinate grid. The UA-ICON horizontal winds and tides have been compared to WACCM-X(SD), GAIA and data from six meteor radars (Stober et al., 2021b). Similar to this study we extracted vertical winds by considering the instrument observation volume.

Figure 6 shows a statistical comparison of hourly retrieved vertical wind velocities for the COL and TDF meteor radars. These histograms are obtained using the entire available data set for both systems, which covers 16 years in the case of COL and about 12 years for TDF. The left column presents the observations from both meteor radars and the right column shows the corresponding UA-ICON data. The histograms exhibit a remarkable agreement of the inferred debiased vertical velocities. The observations, however, indicate more variability compared to the GCM. However, the overall agreement of the vertical velocity distribution between the observations and UA-ICON data reveals that at least the statistical moments of the distributions have significantly improved compared to the least squares derived vertical winds. Furthermore, it is possible to use the skewness of the histogram to estimate potential systematic issues of the radar either due to irregular detections within the radar beam volume or issues in the interferometric solution (e.g., technical problems). Although the debiasing seems to provide reasonable results, we cannot assess the reliability of individual observations or identify other systematic effects due to ~~the~~ other more complicated scattering process (e.g., fragmentation, differential ablation and so forth). Thus, we intend to go beyond these simple approaches and further refine the retrievals to implement physically and mathematically consistent solvers to infer more reliable vertical wind velocities and vertical wind variability.

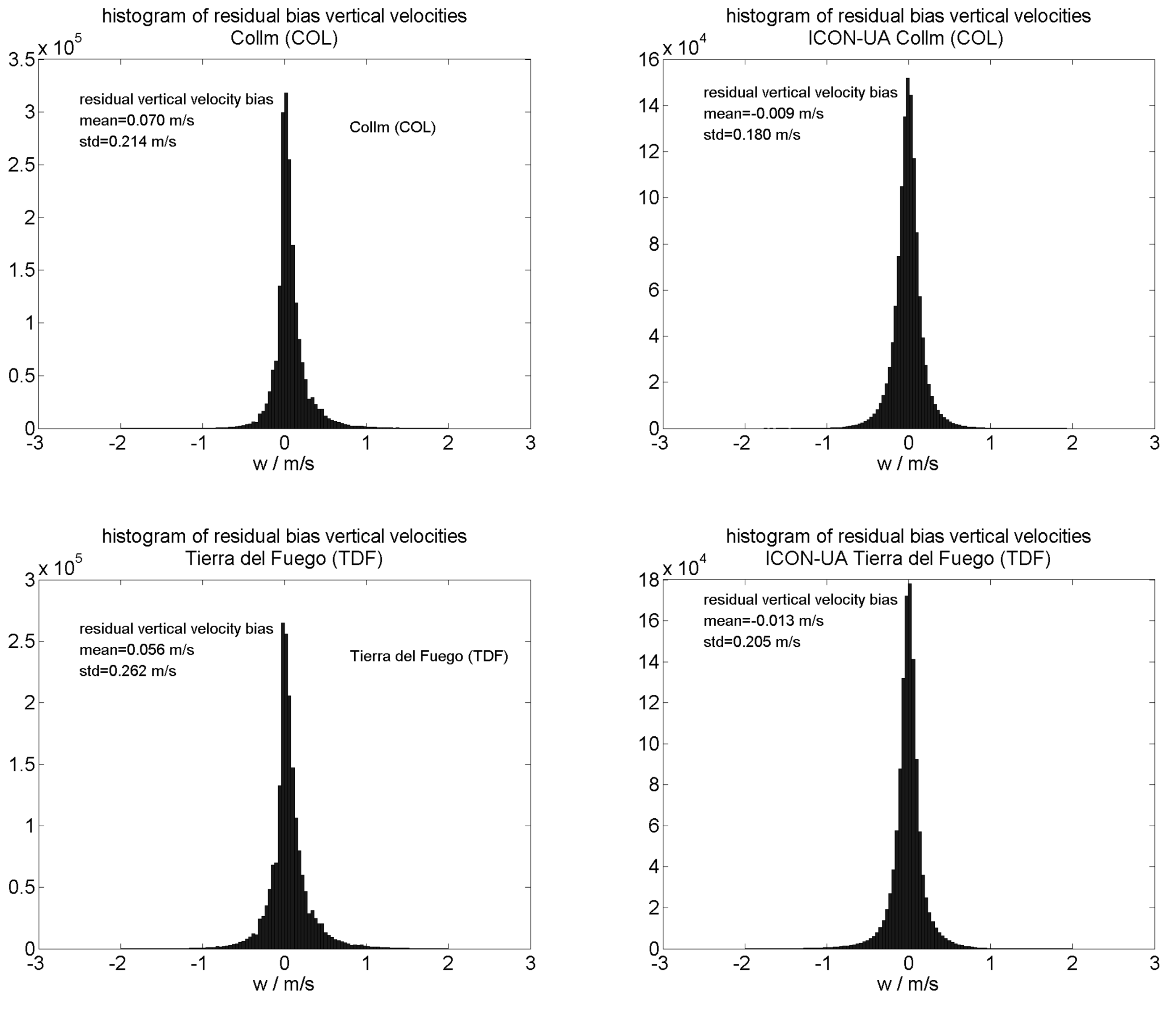

Figure 6. Histograms of the residual vertical velocity for the available data at COL and TDF including the debiasing from the spatio-temporal Laplace filter. The left panels show the meteor radar observations. The right panels visualize the corresponding UA-ICON velocities for a typical meteor radar sampling volume.

6 3DVAR+DIV retrieval

Recently, a 3DVAR algorithm was introduced to retrieve spatially resolved 3D winds using multistatic meteor radar observations from the Nordic Meteor Radar Cluster and CONDOR (Stober et al., 2021a). This 3DVAR algorithm already included the retrieval of vertical winds, but required a Tikhonov regularization to reduce the numerical instabilities, which often arise for parameters with low/poor measurement response. Due to the much worse statistics per grid cell, the quality of each radial velocity measurement comes even more into play and we have to consider the representativeness of a single measurement. This is achieved by introducing a smoothness constraint or variable correlation lengths inside the domain. Such correlation lengths are described by the averaging kernel. However, the zonal and meridional wind components exhibited a reasonable measurement response inside the retrieval domain with values beyond 0.6 and more, indicating short correlations or narrow averaging kernels. Another benefit of the 3DVAR approach was the possibility to add additional constraints by expanding the cost function, e.g., for data assimilation of other observations.

The new 3DVAR+DIV algorithm was revised and expanded by adding a divergence constraint to the cost function. For this, we implemented diagnostics to estimate the horizontal divergence and relative vorticity for each grid cell. We consider that an air parcel that is moved by neutral winds should satisfy the continuity equation;

$$\frac{\partial \rho}{\partial t}\frac{d\rho}{dt} + \rho \cdot div(\mathbf{u}) = 0 \quad . \tag{4}$$

Here ρ is the mass density of the air and we define a density operator in the following way;

$$\frac{d\rho}{dt} = \frac{\partial \rho}{\partial t} + \mathbf{u} \cdot div(\rho) \quad . \tag{5}$$

The spatial and temporal derivatives of the atmospheric density reflect the changes in temperature and pressure of an air parcel when a gravity wave or a whole gravity wave spectra is present within the retrieval domain. Furthermore, the relative importance of each term in the continuity equation depends on the gravity wave properties. We performed a scale analysis for medium frequency gravity waves ($N >> \hat{\omega} >> f$) and estimated the deviation from the incompressible condition using the polarization relations given in Fritts et al. (2002); Hocking et al. (2016). Here N denotes the Brunt-Väisälä frequency, $\hat{\omega}$ is the intrinsic wave period and f is the Coriolis parameter. The non-stationary and compressible terms are in the order of a few percent compared to $\rho \cdot div(\mathbf{u})$-term, which dominates by at least one or two orders of magnitude. More details are given in Appendix **??**. Having performed the scale analysis, it is reasonable to assume a stationary process for each time step, which is equivalent to $\partial\rho/\partial t = 0$$d\rho/dt = 0$. Thus, the continuity equation simplifies and we only have to derive the divergence for each voxel. The divergence is given in Cartesian coordinates by;

$$div(\mathbf{u}) = \frac{\partial u}{\partial x} + \frac{\partial v}{\partial y} + \frac{\partial w}{\partial z} = 0 \quad . \tag{6}$$

In the 3DVAR algorithm, variable domain geometries could be used (Stober et al., 2021a). Therefore, the numerical solution of the derivatives to diagnose the horizontal divergence uses a first order approximation of the elliptical integrals for the WGS84 reference coordinate systems (National Imagery and Mapping Agency, 2000), which appears to be sufficient for most of the typical voxel sizes of a few tens to hundreds of kilometers or a few degrees in latitude and longitude.

Assuming an incompressible flow, we can estimate the change of the vertical velocity Δw between two vertical layers and for each grid cell by;

$$\Delta w_i = \int_{z_1}^{z_2} div \cdot v_{h_i} \;\; dz \quad . \tag{7}$$

Here the index i denotes the grid cell within a layer, and z_1 and z_2 are the upper and lower boundaries, respectively, describing the layer thickness.

The 3DVAR+DIV algorithm solves all equations through several iterations. The first call is again the standard 2DVAR retrieval, which permits us to obtain a first estimate of the horizontal divergence, which can be integrated for each grid cell assuming a lower boundary of the vertical velocity $w(z_0)_{0_i}$. From the second iteration, we include the continuity equation and perform the full 3DVAR+DIV retrieval.

To solve for the vertical velocity at each altitude and grid cell, we need to integrate equation (6) from below or above, which requires an initial value $w(z_0)_{0_i}$. Equation (6) only provides a relative measure for the change of the vertical velocity between two layers. The standard retrieval estimates this boundary in such a way that the mean vertical velocity (integrated over all altitudes) in each column for a defined domain grid is zero. This is equivalent to the assumption that the mean vertical motion in the column over large areas and a vertical dimension of approximately 20-40 km (thickness of meteor layer) is close to zero. However, the 3DVAR algorithm already included the full 3D wind solution for each grid and we just removed the Tikhonov regularization, which damped the numerical instabilities, in the new 3DVAR+DIV retrieval. These vertical velocities are called compressible/non-stationary solution, because we permit at least some deviation from zero in equation (5) without defining an explicit threshold. The major advantage of the 3DVAR+DIV retrieval is now given by providing a compressible/non-stationary and incompressible solution for the vertical velocity for each grid cell. The incompressible solution only makes use of the vertical velocity gradient obtained from the horizontal divergence equation to minimize the numerical instabilities caused by the low geometric measurement response in large parts of the domain. Thus, both solutions exhibit very similar morphology and only show some deviations in the absolute magnitude.

7 Results

The new 3DVAR+DIV retrieval is now implemented for routine data analysis for the Nordic Meteor Radar Cluster and CONDOR. The main goal was to infer more reliable vertical velocities using a more ~~physical~~ physically consistent data description in the forward model. The performance of the new algorithm is demonstrated using observations conducted during September 2021 after major upgrades of the TRO meteor radar. During this time of the year the circulation changes from typical summer conditions to the winter regime. There is a moderate gravity wave activity, and enhanced semidiurnal tides are present (e.g., Wilhelm et al., 2019; Stober et al., 2021b).

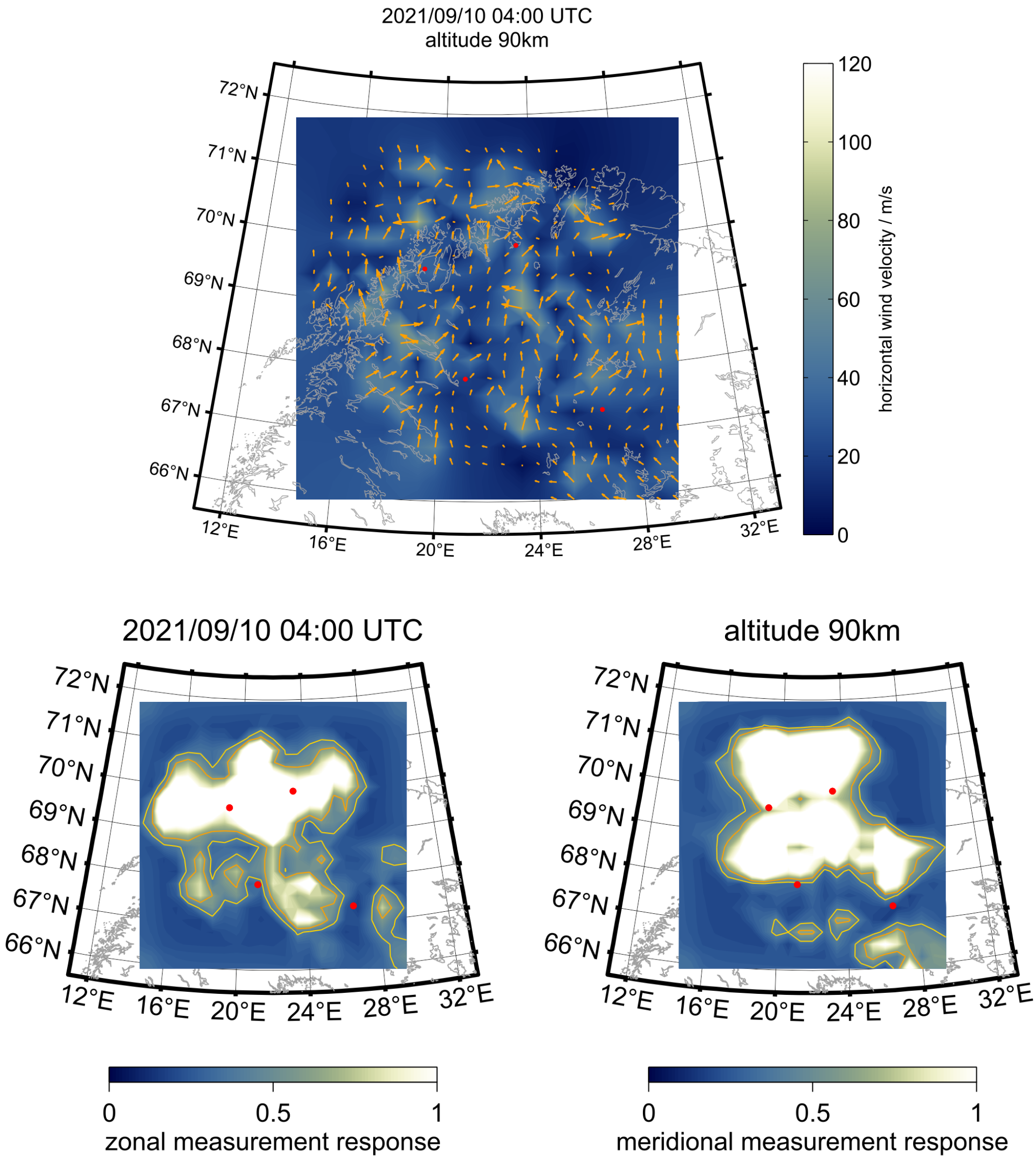

Figure 7. Snapshot of zonal and meridional winds and corresponding measurement response using the 3DVAR+DIV algorithm and measurements from the Nordic Meteor Radar Cluster. The red dots label the locations of the meteor radars. The higher measurement response the better and the more bright are the colors. Bluish colors refer to long correlations, poor measurement statistics and almost no information gain about small scale dynamics.

The results presented herein are based on the 3DVAR+DIV algorithm using the Cartesian geographic grid with 30 km horizontal spacing and WGS84 geometry with a temporal resolution of one hour and a vertical spacing of 2 km. Figure 7 shows four panels. The upper two panels present the zonal (left) and meridional (right) wind components for a single time bin and the

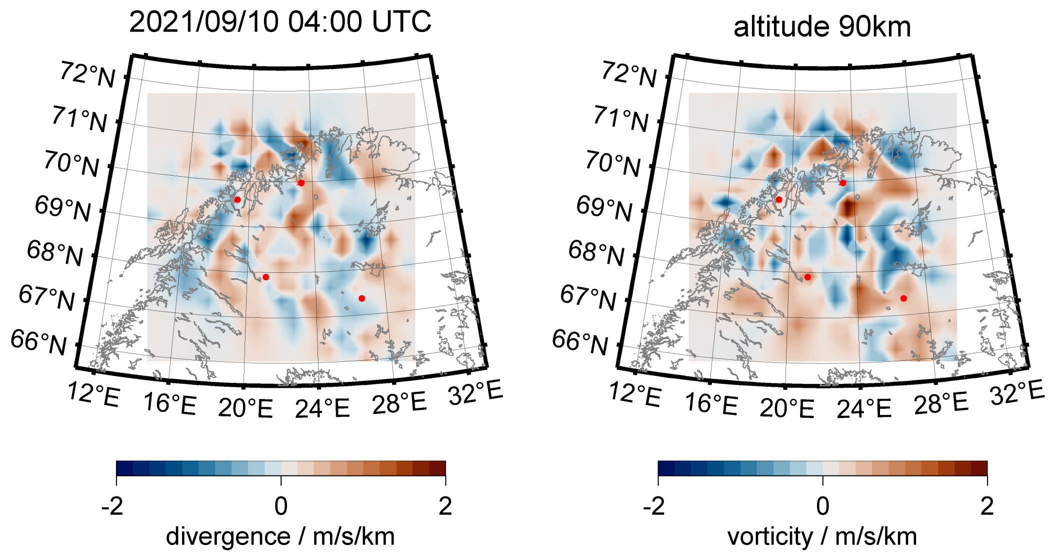

Figure 8. Horizontal divergence and relative vorticity calculated from the 3DVAR+DIV algorithm making use of the horizontal winds. The shown snapshot corresponds to the same period as in Figure 7.

altitude centered at 90 km. Black arrows represent the (horizontal) wind in grid cells that have enough meteor detections. The wind magnitude for each component is color coded. Reddish colors refer to eastward and northward winds, whereas bluish colors indicate westward or southward motions, respectively. The lower two panels visualize the corresponding measurement response (Shannon, 1948; Shannon and Weaver, 1949; Stober et al., 2021a). The whiter the color, the higher is the observation density, which allows ~~to achieve~~ for a high spatial resolution to be achieved. The bluer the grid cells are, the more information is mixed from long distance correlations beyond the next neighboring grid cells corresponding to broader averaging kernels.

An essential improvement of the new 3DVAR+DIV algorithm is the embedded diagnostics of the horizontal divergence and relative vorticity between grid cells. These values are obtained by spatial derivatives qualitatively and quantitatively for all possible geometries and in both implemented domain grids (geographic and Cartesian (rectangular grid)). We use Euler steps at the domain edges and central differences for all other grid cells within the domain. Figure 8 shows the horizontal divergence (left panel) and relative vorticity (right panel) for the same altitude and time period as the winds shown previously. The horizontal divergence exhibits coherent structures that are likely associated with a superposition of several gravity waves. A more random pattern is reflected by the relative vorticity, which shows a more patchy and irregular structure. Both quantities reach a relative strength of about $\pm 2\,\mathrm{m/s/km}$, and occasionally higher values were also found.

Finally, the retrieved vertical velocities (upper panels) and corresponding measurement response (lower panels) are shown in Figure 9. The absolute vertical velocities are obtained assuming a lower boundary, which was determined in such a way that the mean vertical velocity in the column above each grid cell is zero. The compressible/non-stationary and incompressible solution for the vertical velocities are almost identical, which is very often the case. As our forward model makes use of the continuity and radial ~~wind~~ velocity equation, we have no independent estimate of the measurement response for the compressible/non-stationary solution and only the residuals of the radial ~~wind~~ velocity equation contribute to the final estimate. ~~Similar~~ Similarly to the monostatic observations, the geometry of the meteor detections is not favorable to infer reliable vertical winds. Adding the continuity equation compensates for that but also dominates the measurement response and the overall contribution of the finally retrieved 3D winds. This is also reflected by the measurement response for the vertical velocities, which is identical for both solutions for the above mentioned reasons, and is dominated by the horizontal velocity measurement responses.

We also investigated the statistical variability of the 3DVAR+DIV derived vertical velocities. Therefore, we analyzed the year 2021 from the Nordic Meteor Radar Cluster and two weeks of data in March 2020 from CONDOR to estimate the statistical moments of the hourly inferred vertical wind measurements. The corresponding histograms are shown in Figure 10. The histograms only contain results for grid cells with a measurement response larger than 0.5 ~~and~~ for the compressible/non-stationary solution. The incompressible solution (vertical(div)) exhibits ~~an approximately 20%~~ a few percent (<11%) reduced standard deviation for the same periods. The offset of the mean from zero is caused by the lower integration boundary condition being determined including all grid-cells and altitudes, while the histograms only ~~show a subset~~ shows a subset for all grid cells with a measurement response larger than 0.5. Furthermore, CONDOR shows a much higher variability compared to the Nordic Meteor Radar Cluster, which suggests that there is an increased gravity wave activity above the Andes. Considering the different amount of data included in the histograms, we do not want to put too much focus on this difference in the vertical wind variability. Both histograms provide a sufficient database to infer the order of magnitude of the vertical wind variability for a 30 km diameter area. Increased variability is expected since this is significantly smaller than the typical monostatic observation volume.

8 Discussion

Vertical velocity measurements at the MLT are still very challenging. Since the first vertical wind observations performed with the Poker Flat MST radar in 1984 (Bal) using meteor echoes and scattering from coherent echoes, there have been many controversial discussions about potential biases. The results indicated a downwelling of about 30 cm/s during the hemispheric summer at mesopause altitudes, whereas theoretical models predicted an upwelling of about 1 cm/s to understand the cold mesopause temperatures (Holton, 1983). However, these observations also confirmed that the meridional winds were

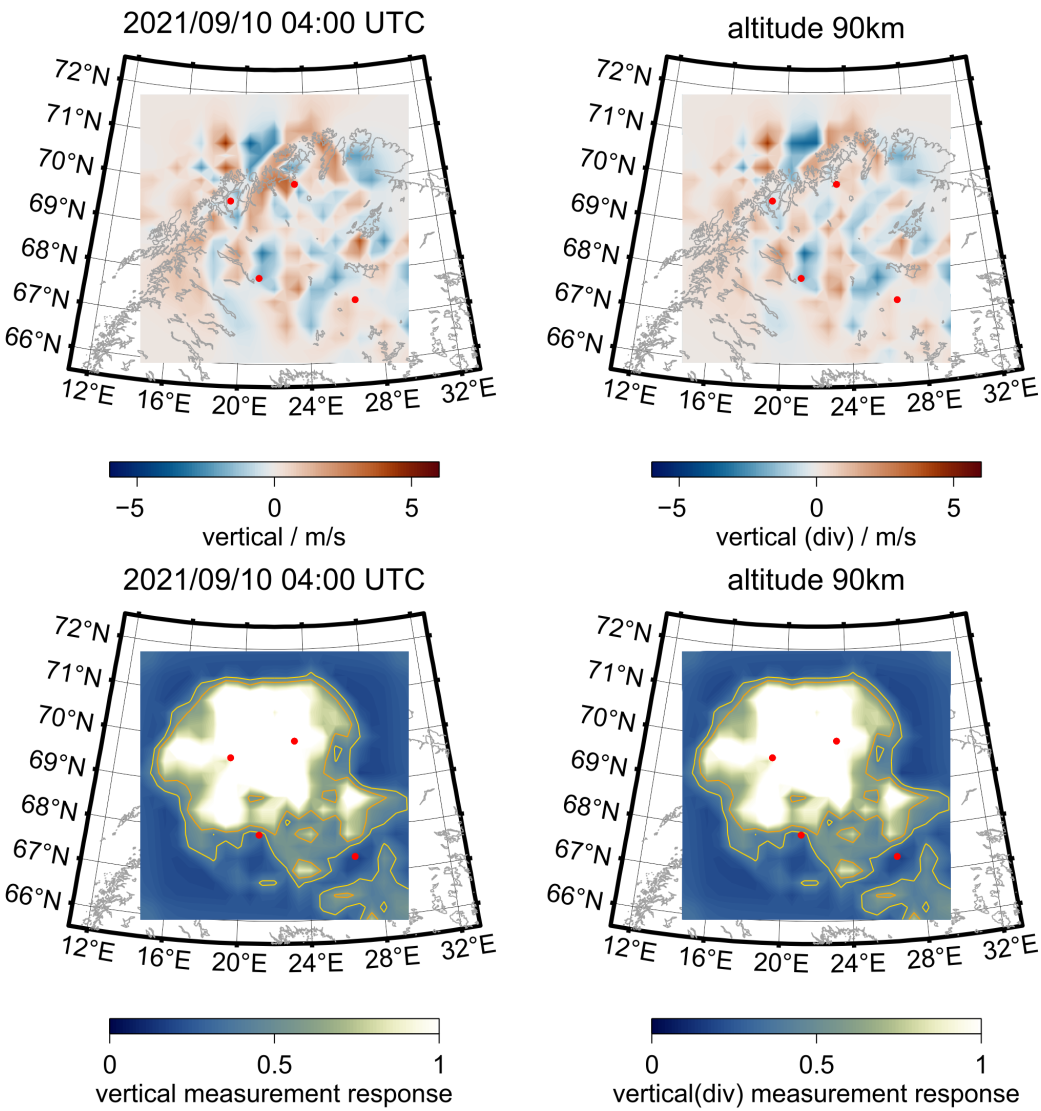

Figure 9. Corresponding vertical wind velocities (upper two panels) (left: compressible/non-stationary solution and right: incompressible solution) and measurement response (lower two panels) obtained by the 3DVAR+DIV algorithm for the same period as Figure 7. Note that the measurement response of the compressible/non-stationary vertical wind solution is dominated by the incompressible solution, which is used in all iterations due to the implemented horizontal divergence constraint.

in agreement with the theory concerning the magnitude and sign. Later, Coy et al. (1986) proposed the Stokes drift to explain these observations, which basically decomposes the motion field in a Lagrangian and a Euler velocity component considering compressibility effects due to gravity waves. However, the Stokes drift depends crucially on the gravity wave properties, which alter the actual trajectory of an air parcel (Walterscheid and Hocking, 1991). Assuming a Garret-Munk type of gravity

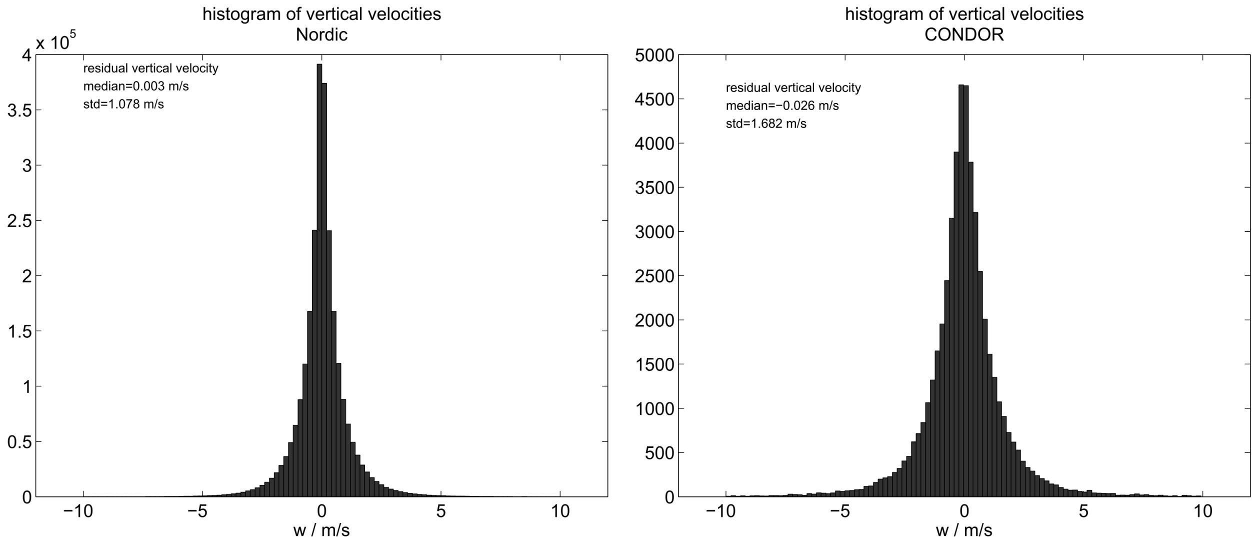

Figure 10. Histograms of hourly vertical winds obtained from the Nordic Meteor Radar Cluster and CONDOR.

wave spectrum the effect of a Stokes drift was estimated to be less than 4 cm/s and, thus, not sufficient to explain the Poker Flat observations (Hall et al., 1992). Furthermore, it was hypothesized that the sedimentation speed of charged ice particles (plasma-laden aerosols) might be more suitable to explain the high negative vertical speeds. The vertical velocities presented here in applying the spatio-temporal Laplace filter and the 3DVAR+DIV algorithm reflect the Euler velocities and can be subject to Stokes drifts, which might explain seasonal differences of the mean velocities, but is less critical for the vertical wind variability considering the results presented in Hall et al. (1992).

The most reliable observations have been carried out with High-Power-Large-Aperture (HPLA) radars such as EISCAT and MAARSY (Hoppe and Fritts, 1995a, b; Fritts et al., 1990; Gudadze et al., 2019). However, these observations still did indicate biases when absolute magnitudes close to zero were tried to be inferred. Some of these biases appear to be caused by gravity waves, as was reported for the EISCAT measurements. MAARSY results indicated a remaining uncertainty due to scattering from PMSE related to the sedimentation speed of the ice particles (Gudadze et al., 2019), which is in agreement to the arguments presented in Hall et al. (1992). However, HPLA radar measurements ~~provides~~ provide at least some valuable insights on the vertical wind variability and the magnitude of the vertical winds for the characteristic beam volumes and dwell times of the systems (seconds to minutes). These radars achieve statistical uncertainties down to a few cm/s of the line of sight velocities, which is sufficient for most geophysical processes (Stober et al., 2018), but still leaves some ambiguities when it comes to the very small vertical velocities related to the residual circulation ~~(e.g., Smith, 2012; Becker, 2012, and references therein)~~ (e.g., Holton, 1983; Smith, 2012; Becker, 2012, and references therein) .

There have been some attempts to derive mean vertical velocities from meteor radar observations applying least squares fits (Egito et al., 2016; Conte et al., 2021). These meteor radar observations clearly exhibit intrinsic biases that can result in artificially large vertical velocities of more than a few m/s. In particular, Conte et al. (2021) reported vertical velocities in the excess of $\pm 10\,\mathrm{m/s}$ over hours. Considering the large observation volume of a few hundreds of kilometers for a typical domain area for multistatic observations these values seem to be very large. Furthermore, based on measurements presented in this study using data from the Nordic Meteor Radar Cluster and CONDOR, we were not able to reproduce these extreme values using the 3DVAR+DIV algorithm analyzing more than 2 years of data. Although there could be various reasons for such large values, we were able to identify some intrinsic biases related to the observation geometry and sampling and present mathematical debiasing strategies for monostatic meteor radars using synthetic data. The proposed Tikhonov regularization and generalized Tikhonov or filter functions provide statistical sound solutions for the vertical winds ~~. However~~mitigating geometrical or numerical issues related to the least squares analysis. Furthermore, we also want to point out that since the assumption of a zero vertical wind seems to be justified in the context of these biases, this approach is mathematical equivalent to a Tikhonov regularization. ~~Furthermore, large biased~~ In addition, artificially large vertical velocities can degrade the quality of the horizontal wind solutions ~~as well~~and also affect other analysis such momentum fluxes.

The comparison of the statistical distribution of ~~the meteor radar inferred vertical velocities~~ vertical velocities inferred from meteor radar observations and the UA-ICON model gives some confidence that the applied debiasing results in more consistent solutions for this wind component. However, there are still some sources of error left ~~,~~ (e.g., fragmentation, motion of scattering center along the trail), which let us conclude that the term 'residual bias vertical velocity' or 'apparent vertical velocity' seems to be the right term as we can not prove the correctness of individual hourly measurements. Fragmentation of the meteoroids and mean winds and wind shears can lead to small changes in the scattering geometry, which cause an apparent shift of the scattering center along the trail. Thus, the Bragg vector of the scattered electromagnetic wave is not necessarily defined by the motion of the trail due to neutral winds. Although these changes appear to be small, they affect the vertical component much more than the horizontal winds. In particular, these apparent motions of the scattering center along the trail could occur for transition echoes from overdense to underdense, which could be caused by fragmentation (Subasinghe et al., 2016; Vida et al., 2021) or by differential ablation (Vondrak et al., 2008).

Almost a decade ago, there was a lidar study on vertical wind magnitudes related to atmospheric tides (Yuan et al., 2014). The climatology exhibited vertical velocities of a few cm/s for large scale atmospheric tidal waves. The lidar observations indicated about 15-20 cm/s vertical wind magnitude for the semidiurnal tide and about 5-10 cm/s for the diurnal tide. These values appear to be consistent with the apparent vertical velocities estimated for the monostatic meteor radars at COL and TDF applying the spatio-temporal Laplace filter. The mid-latitude stations are dominated by semidiurnal tides during the hemispheric winter season and diurnal tides during the summer months (Stober et al., 2021b). However, the vertical wind magnitudes presented by Yuan et al. (2014) and in this study are orders of magnitude lower than other estimates obtained from meteor radar observations (Egito et al., 2016) and multistatic meteor radar data (Chau et al., 2017, 2021; Conte et al., 2021).

Furthermore, we investigated systematic differences in the derived neutral wind velocities using data from CONDOR only. The comparison reveals a considerable difference in the estimated total wind magnitude during several months from May to August at altitudes below 85 km. The difference is most prominently visible in the zonal wind, but also the meridional wind is affected, which is less obvious due to the much lower mean wind speeds. However, our radiant activity mapping of two meteor showers supports the above described scheme of a sliding scattering center or specular point along the meteor trajectory due to the motion of the trail by neutral winds. The source radiant maps only depend on the accurate determination of the pointing direction of the Bragg vector and, thus, are not affected by the apparent scaling of its magnitude due to the sliding of the scattering center along the meteor trajectory. Forward scatter receivers are more prone to this effect. Tiny changes in the geometry result in comparably larger apparent motions of the scattering center compared to monostatic systems. Furthermore, the effect increases the longer the trail lasts, corresponding to a slower diffusion, and, thus, mostly the lower altitudes are affected. However, the discovered bias in CONDOR between the monostatic and forward scatter mean winds is worth to be investigated in more detail and opens the question on how to interpret the Bragg vector and corresponding radial motion concerning the specular or transverse scattering and the meteor trail geometry.

Multistatic observations are versatile and new approaches can be applied to improve vertical wind measurements. Considering the fast development over the past years from the first multistatic forward scatter meteor radar experiment (Stober and Chau, 2015) to more routine and established networks (Chau et al., 2017; Spargo et al., 2019) underlines the huge scientific potential of such observations. These first observations were analyzed making use of the classical assumptions on the vertical velocity ($w = 0\,\mathrm{m/s}$) or by fitting a mean value within the observation volume (Stober and Chau, 2015; Chau et al., 2017). However, the retrieval of vertical winds remained challenging even when more advanced methods were applied (Volz et al., 2021). These advanced methods still resulted in vertical wind velocities of up to 10 m/s and more. The 3DVAR retrieval controlled the numerical instability in the vertical velocities by a Tikhonov regularization for each grid cell (Stober et al., 2021a). The new 3DVAR+DIV approach circumvents the need of an additional Tikhonov regularization by extending the forward model with the continuity equation, which permits to estimate horizontal divergence and relative vorticity directly to constrain the vertical velocity solution.

The algorithm permits us to obtain a compressible/non-stationary and incompressible solution for the vertical winds. Furthermore, the combined radial ~~wind~~ velocity and continuity equations leverage the good measurement response from the horizontal wind velocities, which significantly increases the measurement response for the vertical velocities as well. Due to the much smaller scales that are resolvable with the 3DVAR+DIV retrieval compared to standard monostatic meteor radars, it ~~is also expectable to observe~~ can be expected that a higher variability and larger vertical wind magnitudes might be observable. The values obtained from the new retrieval fit between the large scale values from the monostatic retrievals and observations using HPLA radars (Hoppe and Fritts, 1995a; Fritts et al., 1990; Gudadze et al., 2019), which respresents the limit for the smallest temporal scales of a few seconds (dwell time) and a spatial coverage of 3-4 km (beam diameter). Furthermore, we tested the 3DVAR+DIV retrieval with a much higher temporal resolution of 10 minutes. At this resolution the compressible solution again showed signs of numerical instability due to the much sparser data coverage, which can be compensated by increasing the Lagrange multiplier for the vertical covariance constraint at the cost of smoothing some small scale structures. A similar effect occurs when increasing the vertical bin size beyond the typical 2 km. Due to the large vertical shear often associated ~~due to~~ with large scale waves such as tides, this increases the tendency for numerical instability~~that~~ , which in turn has a negative effect on the reliability of vertical winds.

One aspect is left that is worth ~~to be considered~~consideration. The vertical integration of the horizontal divergence, which is needed to derive absolute vertical velocities, requires an initial boundary condition either at the bottom or top side of the domain depending on the integration direction. Currently this boundary is estimated assuming that the mean vertical velocity in each column above a grid cell is zero. We ~~tested also~~ also tested domain means and other options. These values for the vertical velocity at the lower boundary are typically smaller than $\pm 0.2 - 0.3$ m/s for hourly winds. These vertical velocities are fairly consistent compared to other studies estimating vertical winds at altitudes between 70-80 km altitude (Straub et al., 2012; Vincent et al., 2019), which are representative for a coarser temporal resolution of several hours to a day. Thus, the new 3DVAR+DIV retrieval provides more reliable values of the vertical wind variability rather than absolute wind values at a specific altitude.

Furthermore, the combined horizontal divergence and vertical velocities present ~~a~~ good additional diagnostics to identify coherent structures in the domain area, which can be associated with gravity waves. This is often more difficult to be achieved from the horizontal winds alone without additional filtering. Zonal and meridional winds are dominated by large scale waves such as atmospheric tides that gain large magnitudes and, thus, lead to apparently smooth color maps and mostly parallel wind arrows in the images.

9 Conclusions

In this study we outlined some of the intrinsic biases that arise when inferring vertical winds from standard monostatic and multistatic meteor radar observations. For this purpose, we implemented a data analysis pipeline based on least squares fits with a singular value decomposition solver for real and synthetic data. We demonstrated that even for synthetic data with zero vertical winds in all atmospheric components including mean winds, planetary waves, tides and gravity waves, a least squares analysis results in artificially large vertical winds with a standard deviation of $\pm 2.3\,\mathrm{m/s}$. For real atmospheric soundings the standard deviation had a value of up to $\pm 5\,\mathrm{m/s}$. This bias is caused by the temporal and spatial sampling of meteor radars due to the random occurrence of meteors inside the beam volume of about 350 km in diameter. Every meteor observation is representative for a given time period determined by the decay time of ambipolarly diffusing meteoric plasma and the spatial extension of the scattering volume along the trail. Thus, the apparent line of sight velocities are representative for a well-defined area inside the beam volume defined by the Fresnel scattering and for a very short time period, which is typically less than a second.

Considering these sampling aspects for typical meteor radar observations, we introduced two mathematical debiasing strategies to ensure that the estimated wind components are statistically sound solutions for a given spatial and temporal meteor distribution within each time-altitude bin. We showed that the assumption of a zero vertical wind, which is often used in standard meteor radar wind analysis algorithms, is equivalent to a Tikhonov regularization of the solution for an infinitely large vertical wind component in the Tikhonov matrix. Furthermore, we introduced a more complex approach by designing a spatio-temporal Laplace filter with constraints on the error covariance, which can be seen in the broadest sense as a generalized Tikhonov regularization. This retrieval algorithm resulted in a standard deviation for the same synthetic data set of $\pm 3\,\mathrm{mm/s}$. In addition, we analyzed available multi-year meteor observations from COL and TDF and performed a statistical comparison of the inferred vertical winds with those from the UA-ICON model. The mean and statistical moments of the resultant vertical velocity distributions showed a surprisingly good agreement concerning the GCM. However, we are not able to prove, for individual measurements, the geophysical correctness of the computed vertical wind, which is why we conclude that the term 'residual bias vertical winds' or 'apparent vertical velocity' still seems to be justified.

Although specular or transverse scatter meteor radars have been in use ~~since~~ for decades, there is still some debate about the scattering mechanism and whether there are additional geometry effects due to the high aspect sensitivity of meteor trails. Recent quantitative simulations of reflection coefficients with a full wave scattering model have confirmed a significant change of the effective decay time and signal magnitude, which depends on the polarization of the incident radio wave and the meteor trail alignment (Stober, G. et al., 2021). We were able to identify another bias in the wind magnitude when comparing forward scatter receiver data and monostatic observations using CONDOR. The bias appear to be most significant below 85 km, and increases with decreasing altitude. We explain this offset by a sliding of the scattering center along the meteor trail when the meteoric plasma column ~~is drifted by~~ drifts with the neutral winds. Thus, meteor radars measure the Doppler velocity of the scattering center or specular point, which consists of the 'true' Doppler from the neutral winds and an apparent velocity component caused by an apparent motion of the scattering center along the trail. Source radiant mapping of two meteor showers confirmed that the Bragg vector pointing direction remained unaffected. Most existing meteor radars do not provide information on the meteor orbit or trajectory and, thus, this bias poses an additional challenge to estimate mean vertical winds from monostatic or isolated forward scatter meteor radars. However, for meteor radar networks with overlapping beam volumes the 3DVAR+DIV algorithm compensates some of the remaining issues.

The new 3DVAR+DIV algorithm for multistatic meteor radar networks was implemented for routine data analysis of CONDOR and the Nordic Meteor Radar Cluster observations. This algorithm provides the first physical and mathematical consistent approach to infer vertical velocities and vertical velocity variability from multistatic networks by combining the continuity and radial ~~wind~~ velocity equations in the cost function. Furthermore, the 3DVAR+DIV retrieval includes new diagnostics such as horizontal divergence and relative vorticity for each grid cell. In particular, the horizontal divergence benefits from the good measurement response of the horizontal wind components, and thus, the vertical velocities derived from the incompressible solution are also reflecting a high measurement response. The derived vertical velocities are in the range of $w = 1-2\,\mathrm{m/s}$ and sometimes (3-4 ~~sigma variance~~standard deviation) exceed $3-4\,\mathrm{m/s}$ for single grid cells of 30-by-30 km and a temporal resolution of one hour. Due to the vertical integration of the continuity equation, the absolute magnitude is still subject to the assumption that the mean vertical velocity over a large vertical and spatially column is small. Although the mean absolute value still depends on the upper and lower boundary the horizontal divergence and vertical wind variability are robust quantities and provide valuable information about the spatial scales of gravity waves and their horizontal wavelength spectra. Furthermore, we are able to estimate the degree of deviation from the incompressibility for medium frequency gravity waves leveraging linear theory and polarizuation relations of gravity waves. These deviations were in the order of a few percent and, thus, the 3DVAR+DIV algorithm vertical winds should be reliable and robust and at least provide solutions of the right order of magnitude for retrieved spatial and temporal scales.

Data availability. The data are available upon request. Please contact Alexander Kozlovsky (alexander.kozlovsky@oulu.fi) for the Nordic Meteor Radar Cluster and Alan Liu (LIUZ2@erau.edu) for CONDOR to obtain the 3DVAR+DIV retrievals. The Collm Meteor radar data can be requested from Christoph Jacobi (jacobi@uni-leipzig.de). SAAMER data from Tierra del Fuego can be requested from Diego Janches (diego.janches@nasa.gov).

Appendix A: Scale analysis of compressibility effects in the continuity equation for medium frequency gravity waves

In the following, we are going to briefly outline a scale analysis about the leading terms in the continuity equation to justify the incompressibility constraint and also to estimate the potential deviations for the compressible/non-stationary solution of the vertical winds. This scale analysis is valid for medium frequency gravity waves. A more detailed theoretical description of the fundamental fluid dynamic equations can be found in Holton (1982). Reviews about the linear theory on gravity waves in the middle atmosphere

$$\frac{d\rho}{dt} + \rho \cdot div(\mathbf{u}) = 0 \quad . \tag{A1}$$

$$\frac{\partial\rho}{\partial t} + \mathbf{u} \cdot div(\rho) + \rho \cdot div(\mathbf{u}) = 0 \quad . \tag{A2}$$

Considering that a monochromatic gravity wave can be written as;

$$\rho = \rho' e^{i(kx+mz-\omega t)}, \tag{A3}$$

$$u = u' e^{i(kx+mz-\omega t)},$$

$$v = v' e^{i(kx+mz-\omega t)},$$

$$w = w' e^{i(kx+mz-\omega t)},$$

$$\theta = \theta' e^{i(kx+mz-\omega t)}.$$

Here k is the horizontal wave number, $Theta$ is the potential temperature, m is the vertical wave number, which can be complex and ω describes the intrinsic wave angular frequency. The quantities $\rho', u', v', w', \theta'$ denote the wave amplitude. Furthermore, we introduce a background atmospheric density ρ_0, potential temperature Θ_0 and a wind field $\mathbf{u}_0$. When we now insert the Ansatz of a monochromatic wave in the continuity equation, we obtain;

$$-i\omega\rho' + \mathbf{u}_0(ik\rho' + im\rho') + \rho_0(iku' + imw') = 0 \quad . \tag{A4}$$

Furthermore, we make use of the fundamental fluid dynamic equations for a uniform hydrostatic background state;

$$\frac{d}{dt}\frac{\theta}{\theta_0} + w'\frac{N^2}{g} = 0 \quad . \tag{A5}$$

Considering the relation between potential temperature, pressure and density;

$$\frac{\theta}{\theta_0} = \frac{1}{c_s^2}\frac{p}{p_0} - \frac{\rho}{\rho_0} \quad , \tag{A6}$$

and taking the $\lim_{c_s \to \infty} \frac{1}{c_s^2} = 0$ results in;

$$\frac{1}{\rho_0}\frac{d}{dt}\rho + w'\frac{N^2}{g} = 0 \quad . \tag{A7}$$

Using solutions of a monochromatic gravity wave in equation A7, we find;

$$i\omega\frac{\rho'}{\rho_0} + w'\frac{N^2}{g} = 0 \quad . \tag{A8}$$

Now we focus on a comparison of the amplitudes between the density variation and the vertical winds and we make use of the polarisation relation for a medium frequency gravity wave according to linear theory (Fritts et al., 2002; Hocking et al., 2016), which leads to the following relation;

$$\rho' = \frac{ku'N^2}{m\omega g}\rho_0 \quad . \tag{A9}$$

Finally, we can insert equation A9 in equation A10 and express all terms in dependence of the intrinsic wave properties assuming a background wind field in the form $\mathbf{u}_0 = (u_0, 0, 0)$ and furthermore, we assume that the mean zonal background wind is comparable to the gravity wave fluctuation ($u_0 \approx u'$), which simplifies the final scale analysis, but has no impact on the results. Neglecting the mean vertical wind has also no impact as at most this term could gain the same magnitude as the horizontal wind component. Considering these background boundary conditions in eq. A10, we obtain;

$$\underbrace{\frac{\omega u' N}{g}}_{A} + \underbrace{\frac{k u'^2 N}{g}}_{B} + \underbrace{2u'k}_{C} = 0 \quad . \tag{A10}$$

Finally, we estimate the relative importance of the terms A, B, and C. The term A/C is comparably small for all medium frequency gravity waves and remains below 1% and only gains a relative importance of up to 10% for wave periods approaching the Brunt-Väisälä frequency. However, such gravity waves fall no longer into the medium frequency range and, thus, need to be considered for much higher temporal resolution retrievals than those presented herein. The ratio B/C is basically not exceeding 3% over a wide range of horizontal wavelengths between 30-1000 km and the background atmospheric conditions at the mesosphere and lower thermosphere.

Appendix B: Source radiant

The location of both meteor showers on the celestial sphere was determined using the tracking algorithm presented in Stober et al. (2013) . The error bars denote the width of the stream corresponding to the full-width-half maximum. The mean difference between the right ascension and declination is less than 2 degree and there is no additional dispersion visible when comparing the monostatic meteor radar observations and the passive receivers. Figure B1 was obtained using all solar longitudes with a meteor shower activity exceeding 100 in arbitrary units. Hence, there are also solar longitudes included were the shower was only visible in one of the systems. The radiant motion in celestial coordinates shows the typical shower drift with time and solar longitude (data not shown).

Author contributions. GS and AL developed the idea to include the continuity equation into the 3DVAR algorithm. CM conceptualized the scattering schemes. AK, AL, ZQ, CJ, DJ, GL supported the implementation of the algorithms and data handling of the Nordic Meteor Radar Cluster and CONDOR as well as the Collm and Tierra del Fuego MR (SAAMER). JK, EB, SN, MT, NM, NG, and ML sustained the observations of the Nordic meteor radars and provided the data. HS guided the use of the UA-ICON data analysis and model description. AK reduced the UA-ICON data and performed the analysis including the observational filter. All authors helped with the editing of the manuscript.

Competing interests. The authors declare no competing interests.

Disclaimer. Any opinions, findings, and conclusions or recommendations expressed in this material are those of the author(s) and do not necessarily reflect the views of the National Science Foundation.

Acknowledgements. Gunter Stober is member of the Oeschger Center for Climate Change Research (OCCR). The work by Alan Liu is supported by (while serving at) the National Science Foundation (NSF), USA. Zishun Qiao and the operation of the CONDOR meteor radar system is supported by the NSF grant 1828589. CM is grateful for the logistical support of the Institute of Space and Atmospheric Studies at the University of Saskatchewan. Ales Kuchar and Christoph Jacobi acknowledge support by the Deutsche Forschungsgemeinschaft through grant no. JA 836/43-1. Diego Janches was supported by the NASA Heliophysics ISFM program. TDF's operation is supported by NASA NESC assessment TI-17-01204. This work was supported in part by the NASA Meteoroid Environment Office under cooperative agreement no. 80NSSC18M0046. The Esrange meteor radar operation, maintenance and data collection were provided by the Esrange Space Center of the Swedish Space Corporation. The 3D-Var retrievals were developed as part of the ARISE design study (http://arise-project.eu/, last access: 8 October 2020) funded by the European Union's Seventh Framework Programme for Research and Technological Development. This research has been supported by the STFC (grant no. ST/S000429/1 to Mark Lester). This study is partly supported by Grants-in-Aid for Scientific Research (no. 17H02968) of the Japan Society for the Promotion of Science (JSPS). We thank Hauke Schmidt (Max Planck Institute for Meteorology) for providing the UA-ICON output. Njal Gulbrandsen acknowledges the support of the Leibniz-Institute of Atmospheric Physics (IAP), Kühlungsborn, Germany for their contributions to the upgrade of the TRO meteor radar.

References

Andrioli, V. F., Fritts, D. C., Batista, P. P., and Clemesha, B. R.: Improved analysis of all-sky meteor radar measurements of gravity wave variances and momentum fluxes, Annales Geophysicae, 31, 889–908, https://doi.org/10.5194/angeo-31-889-2013, 2013.

Batista, P., Clemesha, B., Tokumoto, A., and Lima, L.: Structure of the mean winds and tides in the meteor region over Cachoeira Paulista, Brazil (22.7°S,45°W) and its comparison with models, Journal of Atmospheric and Solar-Terrestrial Physics, 66, 623 – 636, https://doi.org/https://doi.org/10.1016/j.jastp.2004.01.014, dynamics and Chemistry of the MLT Region - PSMOS 2002 International Symposium, 2004.

Becker, E.: Dynamical Control of the Middle Atmosphere, Space Science Reviews, 168, 283–314, https://doi.org/10.1007/s11214-011-9841-5, 2012.

Becker, E. and Vadas, S. L.: Secondary Gravity Waves in the Winter Mesosphere: Results From a High-Resolution Global Circulation Model, Journal of Geophysical Research: Atmospheres, 123, 2605–2627, https://doi.org/10.1002/2017JD027460, 2018.

Borchert, S., Zhou, G., Baldauf, M., Schmidt, H., Zängl, G., and Reinert, D.: The upper-atmosphere extension of the ICON general circulation model (version: ua-icon-1.0), Geoscientific Model Development, 12, 3541–3569, https://doi.org/10.5194/gmd-12-3541-2019, 2019.

Brown, P., Weryk, R., Wong, D., and Jones, J.: A meteoroid stream survey using the Canadian Meteor Orbit Radar: I. Methodology and radiant catalogue, Icarus, 195, 317–339, https://doi.org/https://doi.org/10.1016/j.icarus.2007.12.002, 2008a.

Brown, P., Wong, D., Weryk, R., and Wiegert, P.: A meteoroid stream survey using the Canadian Meteor Orbit Radar: II: Identification of minor showers using a 3D wavelet transform, Icarus, 207, 66–81, https://doi.org/https://doi.org/10.1016/j.icarus.2009.11.015, 2010.

Brown, P. G., Weryk, R., Wong, D., and Jones, J.: A meteoroid stream survey using the Canadian Meteor Orbit Radar I. Methodology and radiant catalogue, Icarus, 195, 317–339, https://doi.org/10.1016/j.icarus.2007.12.002, 2008b.

Chau, J. L., Stober, G., Hall, C. M., Tsutsumi, M., Laskar, F. I., and Hoffmann, P.: Polar mesospheric horizontal divergence and relative vorticity measurements using multiple specular meteor radars, Radio Science, pp. n/a–n/a, https://doi.org/10.1002/2016RS006225, 2016RS006225, 2017.

Chau, J. L., Urco, J. M., Vierinen, J., Harding, B. J., Clahsen, M., Pfeffer, N., Kuyeng, K. M., Milla, M. A., and Erickson, P. J.: Multistatic Specular Meteor Radar Network in Peru: System Description and Initial Results, Earth and Space Science, 8, e2020EA001 293, https://doi.org/https://doi.org/10.1029/2020EA001293, e2020EA001293 2020EA001293, 2021.

Conte, J. F., Chau, J. L., Urco, J. M., Latteck, R., Vierinen, J., and Salvador, J. O.: First Studies of Mesosphere and Lower Thermosphere Dynamics Using a Multistatic Specular Meteor Radar Network Over Southern Patagonia, Earth and Space Science, 8, e2020EA001 356, https://doi.org/https://doi.org/10.1029/2020EA001356, e2020EA001356 2020EA001356, 2021.

Coy, L., Fritts, D. C., and Weinstock, J.: The Stokes Drift due to Vertically Propagating Internal Gravity Waves in a Compressible Atmosphere, Journal of Atmospheric Sciences, 43, 2636 – 2643, https://doi.org/10.1175/1520-0469(1986)043<2636:TSDDTV>2.0.CO;2, 1986.

Crueger, T., Giorgetta, M. A., Brokopf, R., Esch, M., Fiedler, S., Hohenegger, C., Kornblueh, L., Mauritsen, T., Nam, C., Naumann, A. K., et al.: ICON-A, The atmosphere component of the ICON Earth system model: II. Model evaluation, Journal of Advances in Modeling Earth Systems, 10, 1638–1662, 2018.

de Araújo, L. R., Lima, L. M., Batista, P. P., and Jacobi, C.: Behaviour of monthly tides from meteor radar winds at 22.7°S during declining phases of 23 and 24 solar cycles, Journal of Atmospheric and Solar-Terrestrial Physics, 205, 105 298, https://doi.org/https://doi.org/10.1016/j.jastp.2020.105298, 2020.

de Wit, R. J., Hibbins, R. E., Espy, P. J., Orsolini, Y. J., Limpasuvan, V., and Kinnison, D. E.: Observations of gravity wave forcing of the mesopause region during the January 2013 major Sudden Stratospheric Warming, Geophysical Research Letters, 41, 4745–4752, https://doi.org/10.1002/2014GL060501, 2014.

Eckermann, S. D., Ma, J., Hoppel, K. W., Kuhl, D. D., Allen, D. R., Doyle, J. A., Viner, K. C., Ruston, B. C., Baker, N. L., Swadley, S. D., Whitcomb, T. R., Reynolds, C. A., Xu, L., Kaifler, N., Kaifler, B., Reid, I. M., Murphy, D. J., and Love, P. T.: High-Altitude (0-100 km) Global Atmospheric Reanalysis System: Description and Application to the 2014 Austral Winter of the Deep Propagating Gravity Wave Experiment (DEEPWAVE), Monthly Weather Review, 146, 2639–2666, https://doi.org/10.1175/MWR-D-17-0386.1, 2018.

Egito, F., Andrioli, V., and Batista, P.: Vertical winds and momentum fluxes due to equatorial planetary scale waves using all-sky meteor radar over Brazilian region, Journal of Atmospheric and Solar-Terrestrial Physics, 149, 108 – 119, https://doi.org/https://doi.org/10.1016/j.jastp.2016.10.005, 2016.

Franke, S. J., Chu, X., Liu, A. Z., and Hocking, W. K.: Comparison of meteor radar and Na Doppler lidar measurements of winds in the mesopause region above Maui, Hawaii, J. Geophys. Res., 110, D09S02, https://doi.org/10.1029/2003JD004486, 2005.

Fritts, D., Hoppe, U.-P., and Inhester, B.: A study of the vertical motion field near the high-latitude summer mesopause during MAC/SINE, Journal of Atmospheric and Terrestrial Physics, 52, 927–938, https://doi.org/https://doi.org/10.1016/0021-9169(90)90025-I, middle atmosphere dynamics at high latitudes, 1990.

Fritts, D. C., Vadas, S. L., and Yamada, Y.: An estimate of strong local body forcing and gravity wave radiation based on OH airglow and meteor radar observations, Geophysical Research Letters, 29, 71–1–71–4, https://doi.org/10.1029/2001GL013753, 2002.

Fritts, D. C., Janches, D., and Hocking, W. K.: Southern Argentina Agile Meteor Radar: Initial assessment of gravity wave momentum fluxes, Journal of Geophysical Research: Atmospheres, 115, n/a–n/a, https://doi.org/10.1029/2010JD013891, d19123, 2010a.

Fritts, D. C., Janches, D., Iimura, H., Hocking, W. K., Mitchell, N. J., Stockwell, R. G., Fuller, B., Vandepeer, B., Hormaechea, J., Brunini, C., and Levato, H.: Southern Argentina Agile Meteor Radar: System design and initial measurements of large-scale winds and tides, Journal of Geophysical Research: Atmospheres, 115, https://doi.org/10.1029/2010JD013850, 2010b.

Gelaro, R., McCarty, W., Suárez, M. J., Todling, R., Molod, A., Takacs, L., Randles, C. A., Darmenov, A., Bosilovich, M. G., Reichle, R., Wargan, K., Coy, L., Cullather, R., Draper, C., Akella, S., Buchard, V., Conaty, A., da Silva, A. M., Gu, W., Kim, G.-K., Koster, R., Lucchesi, R., Merkova, D., Nielsen, J. E., Partyka, G., Pawson, S., Putman, W., Rienecker, M., Schubert, S. D., Sienkiewicz, M., and Zhao, B.: The Modern-Era Retrospective Analysis for Research and Applications, Version 2 (MERRA-2), Journal of Climate, 30, 5419 – 5454, https://doi.org/10.1175/JCLI-D-16-0758.1, 2017.

Giorgetta, M. A., Brokopf, R., Crueger, T., Esch, M., Fiedler, S., Helmert, J., Hohenegger, C., Kornblueh, L., Köhler, M., Manzini, E., et al.: ICON-A, the atmosphere component of the ICON Earth System Model: I. Model description, Journal of Advances in Modeling Earth Systems, 10, 1613–1637, 2018.

Gudadze, N., Stober, G., and Chau, J. L.: Can VHF radars at polar latitudes measure mean vertical winds in the presence of PMSE?, Atmospheric Chemistry and Physics, 19, 4485–4497, https://doi.org/10.5194/acp-19-4485-2019, 2019.

Guo, Y. and Liu, A. Z.: Seasonal variation of vertical heat and energy fluxes due to dissipating gravity waves in the mesopause region over the Andes, J. Geophys. Res. Atmos., 126, e2020JD033 825, https://doi.org/10.1029/2020JD033825, 2021.

Hall, T. M., Cho, J. Y. N., Kelley, M. C., and Hocking, W. K.: A re-evaluation of the Stokes drift in the polar summer mesosphere, Journal of Geophysical Research: Atmospheres, 97, 887–897, https://doi.org/https://doi.org/10.1029/91JD02835, 1992.

Hocking, W.: Spatial distribution of errors associated with multistatic meteor radar, Earth Planets Space, 70, https://doi.org/https://doi.org/10.1186/s40623-018-0860-2, 2018.

Hocking, W., Fuller, B., and Vandepeer, B.: Real-time determination of meteor-related parameters utilizing modern digital technology, Journal of Atmospheric and Solar-Terrestrial Physics, 63, 155 – 169, https://doi.org/http://dx.doi.org/10.1016/S1364-6826(00)00138-3, radar applications for atmosphere and ionosphere research - PIERS 1999, 2001.

Hocking, W. K.: Real-time meteor entrance speed determinations made with interferometric meteor radars, Radio Science, 35, 1205–1220, https://doi.org/https://doi.org/10.1029/1999RS002283, 2000.

Hocking, W. K. and Thayaparan, T.: Simultaneous and colocated observation of winds and tides by MF and meteor radars over London, Canada (43°N, 81°W), during 1994–1996, Radio Science, 32, 833–865, https://doi.org/https://doi.org/10.1029/96RS03467, 1997.

Hocking, W. K., Thayaparan, T., and Jones, J.: Meteor decay times and their use in determining a diagnostic mesospheric Temperature-pressure parameter: Methodology and one year of data, Geophysical Research Letters, 24, 2977–2980, https://doi.org/10.1029/97GL03048, 1997.

Hocking, W. K., Röttger, J., Palmer, R. D., Sato, T., and Chilson, P. B.: Atmospheric Radar: Application and Science of MST Radars in the Earth's Mesosphere, Stratosphere, Troposphere, and Weakly Ionized Regions, Cambridge University Press, https://doi.org/10.1017/9781316556115, 2016.

Hoffmann, P., Singer, W., Keuer, D., Hocking, W., Kunze, M., and Murayama, Y.: Latitudinal and longitudinal variability of mesospheric winds and temperatures during stratospheric warming events, Journal of Atmospheric and Solar-Terrestrial Physics, 69, 2355–2366, https://doi.org/http://dx.doi.org/10.1016/j.jastp.2007.06.010, vertical Coupling in the Atmosphere/Ionosphere System3rd IAGA/ICMA Workshop, 2007.

Holdsworth, D. A., Reid, I. M., and Cervera, M. A.: Buckland Park all-sky interferometric meteor radar, Radio Science, 39, n/a–n/a, https://doi.org/10.1029/2003RS003014, rS5009, 2004.

Holton, J. R.: The Role of Gravity Wave Induced Drag and Diffusion in the Momentum Budget of the Mesosphere, Journal of Atmospheric Sciences, 39, 791 – 799, https://doi.org/10.1175/1520-0469(1982)039<0791:TROGWI>2.0.CO;2, 1982.

Holton, J. R.: The Influence of Gravity Wave Breaking on the General Circulation of the Middle Atmosphere, Journal of Atmospheric Sciences, 40, 2497 – 2507, https://doi.org/10.1175/1520-0469(1983)040<2497:TIOGWB>2.0.CO;2, 1983.

Hoppe, U.-P. and Fritts, D. C.: High-resolution measurements of vertical velocity with the European incoherent scatter VHF radar: 1. Motion field characteristics and measurement biases, Journal of Geophysical Research: Atmospheres, 100, 16 813–16 825, https://doi.org/https://doi.org/10.1029/95JD01466, 1995a.

Hoppe, U.-P. and Fritts, D. C.: On the downward bias in vertical velocity measurements by VHF radars, Geophysical Research Letters, 22, 619–622, https://doi.org/https://doi.org/10.1029/95GL00165, 1995b.

Jacobi, C., Fröhlich, K., Viehweg, C., Stober, G., and Kürschner, D.: Midlatitude mesosphere/lower thermosphere meridional winds and temperatures measured with meteor radar, Advances in Space Research, 39, 1278–1283, https://doi.org/https://doi.org/10.1016/j.asr.2007.01.003, 2007.

Jacobi, C., Arras, C., Kürschner, D., Singer, W., Hoffmann, P., and Keuer, D.: Comparison of mesopause region meteor radar winds, medium frequency radar winds and low frequency drifts over Germany, Advances in Space Research, 43, 247 – 252, https://doi.org/http://dx.doi.org/10.1016/j.asr.2008.05.009, 2009.

Janches, D., Hormaechea, J., Brunini, C., Hocking, W., and Fritts, D.: An initial meteoroid stream survey in the southern hemisphere using the Southern Argentina Agile Meteor Radar (SAAMER), Icarus, 223, 677–683, https://doi.org/https://doi.org/10.1016/j.icarus.2012.12.018, 2013.

Janches, D., Close, S., Hormaechea, J. L., Swarnalingam, N., Murphy, A., O'Connor, D., Vandepeer, B., Fuller, B., Fritts, D. C., and Brunini, C.: The Southern Argentina Agile Meteor Radar Orbital System (SAAMER-OS): An initial sporadic meteoroid orbital survey in the southern sky, The Astrophysical Journal, 809, 36, https://doi.org/10.1088/0004-637x/809/1/36, 2015.

Jones, J. and Jones, W.: Oblique-scatter of radio waves from meteor trains: Iong wavelength approximation, Planetary and Space Science, 38, 925–932, https://doi.org/https://doi.org/10.1016/0032-0633(90)90059-Y, 1990.

Jones, J. and Jones, W.: Meteor radiant activity mapping using single-station radar observations, Monthly Notices of the Royal Astronomical Society, 367, 1050–1056, https://doi.org/10.1111/j.1365-2966.2006.10025.x, 2006.

Jones, J., Webster, A. R., and Hocking, W. K.: An improved interferometer design for use with meteor radars, Radio Science, 33, 55–65, https://doi.org/10.1029/97RS03050, 1998.

Jones, J., Brown, P. G., Ellis, K. J., Webster, A., Campbell-Brown, M., Krzemenski, Z., and Weryk, R.: The Canadian Meteor Orbit Radar : system overview and preliminary results, Planetary and Space Science, 53, 413–421, https://doi.org/10.1016/j.pss.2004.11.002, 2005.

Larsen, M. F., Liu, A. Z., Bishop, R. L., and Hecht, J. H.: TOMEX: A comparison of lidar and sounding rocket chemical tracer wind measurement, Geophys. Res. Lett., 30, 1375, https://doi.org/10.1029/2002GL015678, 2003.

Latteck, R., Singer, W., Rapp, M., Vandepeer, B., Renkwitz, T., Zecha, M., and Stober, G.: MAARSY: The new MST radar on Andøya—System description and first results, Radio Science, 47, https://doi.org/https://doi.org/10.1029/2011RS004775, 2012.

Liu, A. Z., Lu, X., and Franke, S. J.: Diurnal variation of gravity wave momentum flux and its forcing on the diurnal tide, J. Geophys. Res. Atmos., 118, 1668–1678, https://doi.org/10.1029/2012JD018653, 2013.

Liu, G., Janches, D., Lieberman, R. S., Moffat-Griffin, T., Fritts, D. C., and Mitchell, N. J.: Coordinated Observations of 8- and 6-hr Tides in the Mesosphere and Lower Thermosphere by Three Meteor Radars Near 60°S Latitude, Geophysical Research Letters, 47, e2019GL086 629, https://doi.org/10.1029/2019GL086629, e2019GL086629 2019GL086629, 2020.

Liu, H.-L., McInerney, J. M., Santos, S., Lauritzen, P. H., Taylor, M. A., and Pedatella, N. M.: Gravity waves simulated by high-resolution Whole Atmosphere Community Climate Model, Geophys. Res. Lett., 41, 9106–9112, https://doi.org/10.1002/2014GL062468, 2014.

Mazur, M., Pokorný, P., Brown, P., Weryk, R. J., Vida, D., Schult, C., Stober, G., and Agrawal, A.: Precision Measurements of Radar Transverse Scattering Speeds From Meteor Phase Characteristics, Radio Science, 55, 1–32, https://doi.org/10.1029/2019RS006987, 2020.

McCormack, J., Hoppel, K., Kuhl, D., de Wit, R., Stober, G., Espy, P., Baker, N., Brown, P., Fritts, D., Jacobi, C., Janches, D., Mitchell, N., Ruston, B., Swadley, S., Viner, K., Whitcomb, T., and Hibbins, R.: Comparison of mesospheric winds from a high-altitude meteorological analysis system and meteor radar observations during the boreal winters of 2009-2010 and 2012-2013, Journal of Atmospheric and Solar-Terrestrial Physics, 154, 132 – 166, https://doi.org/http://dx.doi.org/10.1016/j.jastp.2016.12.007, 2017.

McKinley, D. W. R.: Meteor science and engineering., 1961.

Meek, C. E., Manson, A. H., Hocking, W. K., and Drummond, J. R.: Eureka, 80°N, SKiYMET meteor radar temperatures compared with Aura MLS values, Annales Geophysicae, 31, 1267–1277, https://doi.org/10.5194/angeo-31-1267-2013, 2013.

Miyoshi, Y., Pancheva, D., Mukhtarov, P., Jin, H., Fujiwara, H., and Shinagawa, H.: Excitation mechanism of non-migrating tides, J. of Atmospheric and Solar-Terrestrial Physics, 156, 24–36, https://doi.org/https://doi.org/10.1016/j.jastp.2017.02.012, 2017.

National Imagery and Mapping Agency: Department of Defense World Geodetic System 1984: its definition and relationships with local geodetic systems, Tech. Rep. TR8350.2, National Imagery and Mapping Agency, St. Louis, MO, USA, http://earth-info.nga.mil/GandG/publications/tr8350.2/tr8350_2.html, 2000.

Panka, P. A., Weryk, R. J., Bruzzone, J. S., Janches, D., Schult, C., Stober, G., and Hormaechea, J. L.: An Improved Method to Measure Head Echoes Using a Meteor Radar, The Planetary Science Journal, 2, 197, https://doi.org/10.3847/psj/ac22b2, 2021.

Pokorny, P., Janches, D., Brown, P., and Hormaechea, J.: An orbital meteoroid stream survey using the Southern Argentina Agile MEteor Radar (SAAMER) based on a wavelet approach, Icarus, 290, 162–182, https://doi.org/https://doi.org/10.1016/j.icarus.2017.02.025, 2017.

Portnyagin, Y. I., Solovjova, T. V., Makarov, N. A., Merzlyakov, E. G., Manson, A. H., Meek, C. E., Hocking, W., Mitchell, N., Pancheva, D., Hoffmann, P., Singer, W., Murayama, Y., Igarashi, K., Forbes, J. M., Palo, S., Hall, C., and Nozawa, S.: Monthly mean climatology of the prevailing winds and tides in the Arctic mesosphere/lower thermosphere, Annales Geophysicae, 22, 3395–3410, https://doi.org/10.5194/angeo-22-3395-2004, 2004.

Poulter, E. and Baggaley, W.: Radiowave scattering from meteoric ionization, Journal of Atmospheric and Terrestrial Physics, 39, 757 – 768, https://doi.org/https://doi.org/10.1016/0021-9169(77)90137-4, 1977.

Press, W. H., Flannery, B. P., Teukolsky, S. A., and Vetterling, W. T.: Numerical Recipes in FORTRAN 77: The Art of Scientific Computing, Cambridge University Press, 2 edn., http://www.worldcat.org/isbn/052143064X, 1992.

Qian, L., Burns, A., and Yue, J.: Evidence of the lower thermospheric winter-to-summer circulation from SABER CO2 observations, Geophys. Res. Lett., 44, 10,100–10,107, https://doi.org/10.1002/2017GL075643, 2017.

Rhodes, C. T., Shao, X. M., Krehbiel, P. R., Thomas, R. J., and Hayenga, C. O.: Observations of lightning phenomena using radio interferometry, Journal of Geophysical Research: Atmospheres, 99, 13 059–13 082, https://doi.org/https://doi.org/10.1029/94JD00318, 1994.

Schranz, F., Hagen, J., Stober, G., Hocke, K., Murk, A., and Kämpfer, N.: Small-scale variability of stratospheric ozone during the SSW 2018/2019 observed at Ny-Ålesund, Svalbard, Atmospheric Chemistry and Physics Discussions, 2019, 1–25, https://doi.org/10.5194/acp-2019-1093, 2019.

Schult, C., Brown, P., Pokorný, P., Stober, G., and Chau, J. L.: A meteoroid stream survey using meteor head echo observations from the Middle Atmosphere ALOMAR Radar System (MAARSY), Icarus, 309, 177–186, https://doi.org/https://doi.org/10.1016/j.icarus.2018.02.032, 2018.

Shannon, C. E.: A Mathematical Theory of Communication, Bell System Technical Journal, 27, 379–423, https://doi.org/https://doi.org/10.1002/j.1538-7305.1948.tb01338.x, 1948.

Shannon, C. E. and Weaver, W.: The Mathematical Theory of Communication, University of Illinois Press, Urbana, IL, 1949.

Smith, A. K.: Global Dynamics of the MLT, Surveys in Geophysics, 33, 1177–1230, https://doi.org/10.1007/s10712-012-9196-9, 2012.

Smith, A. K., Garcia, R. R., Marsh, D. R., Kinnison, D. E., and Richter, J. H.: Simulations of the response of mesospheric circulation and temperature to the Antarctic ozone hole, Geophys. Res. Lett., 37, L22 803, 2010.

Spargo, A. J., Reid, I. M., and MacKinnon, A. D.: Multistatic meteor radar observations of gravity-wave–tidal interaction over southern Australia, Atmospheric Measurement Techniques, 12, 4791–4812, https://doi.org/10.5194/amt-12-4791-2019, 2019.

Stober, G. and Chau, J. L.: A multistatic and multifrequency novel approach for specular meteor radars to improve wind measurements in the MLT region, Radio Science, 50, 431–442, https://doi.org/10.1002/2014RS005591, 2014RS005591, 2015.

Stober, G., Jacobi, C., Matthias, V., Hoffmann, P., and Gerding, M.: Neutral air density variations during strong planetary wave activity in the mesopause region derived from meteor radar observations, Journal of Atmospheric and Solar-Terrestrial Physics, 74, 55 – 63, https://doi.org/http://dx.doi.org/10.1016/j.jastp.2011.10.007, 2012.

Stober, G., Schult, C., Baumann, C., Latteck, R., and Rapp, M.: The Geminid meteor shower during the ECOMA sounding rocket campaign: specular and head echo radar observations, Annales Geophysicae, 31, 473–487, https://doi.org/10.5194/angeo-31-473-2013, 2013.

Stober, G., Matthias, V., Jacobi, C., Wilhelm, S., Höffner, J., and Chau, J. L.: Exceptionally strong summer-like zonal wind reversal in the upper mesosphere during winter 2015/16, Annales Geophysicae, 35, 711–720, https://doi.org/10.5194/angeo-35-711-2017, 2017.

Stober, G., Sommer, S., Schult, C., Latteck, R., and Chau, J. L.: Observation of Kelvin–Helmholtz instabilities and gravity waves in the summer mesopause above Andenes in Northern Norway, Atmospheric Chemistry and Physics, 18, 6721–6732, https://doi.org/10.5194/acp-18-6721-2018, 2018.

Stober, G., Baumgarten, K., McCormack, J. P., Brown, P., and Czarnecki, J.: Comparative study between ground-based observations and NAVGEM-HA reanalysis data in the MLT region, Atmospheric Chemistry and Physics Discussions, 2019, 1–37, https://doi.org/10.5194/acp-2019-1006, 2019.

Stober, G., Kozlovsky, A., Liu, A., Qiao, Z., Tsutsumi, M., Hall, C., Nozawa, S., Lester, M., Belova, E., Kero, J., Espy, P. J., Hibbins, R. E., and Mitchell, N.: Atmospheric tomography using the Nordic Meteor Radar Cluster and Chilean Observation Network De Meteor Radars: network details and 3D-Var retrieval, Atmospheric Measurement Techniques, 14, 6509–6532, https://doi.org/10.5194/amt-14-6509-2021, 2021a.

Stober, G., Kuchar, A., Pokhotelov, D., Liu, H., Liu, H.-L., Schmidt, H., Jacobi, C., Baumgarten, K., Brown, P., Janches, D., Murphy, D., Kozlovsky, A., Lester, M., Belova, E., Kero, J., and Mitchell, N.: Interhemispheric differences of mesosphere–lower thermosphere winds and tides investigated from three whole-atmosphere models and meteor radar observations, Atmospheric Chemistry and Physics, 21, 13 855–13 902, https://doi.org/10.5194/acp-21-13855-2021, 2021b.

Stober, G., Brown, P., Campbell-Brown, M., and Weryk, R. J.: Triple-frequency meteor radar full wave scattering - Measurements and comparison to theory, A&A, 654, A108, https://doi.org/10.1051/0004-6361/202141470, 2021.

Straub, C., Tschanz, B., Hocke, K., Kämpfer, N., and Smith, A. K.: Transport of mesospheric H_2O during and after the stratospheric sudden warming of January 2010: observation and simulation, Atmospheric Chemistry and Physics, 12, 5413–5427, https://doi.org/10.5194/acp-12-5413-2012, 2012.

Subasinghe, D., Campbell-Brown, M. D., and Stokan, E.: Physical characteristics of faint meteors by light curve and high-resolution observations, and the implications for parent bodies, Monthly Notices of the Royal Astronomical Society, 457, 1289–1298, https://doi.org/10.1093/mnras/stw019, 2016.

Vida, D., Brown, P. G., Campbell-Brown, M., Weryk, R. J., Stober, G., and McCormack, J. P.: High precision meteor observations with the Canadian automated meteor observatory: Data reduction pipeline and application to meteoroid mechanical strength measurements, Icarus, 354, 114 097, https://doi.org/https://doi.org/10.1016/j.icarus.2020.114097, 2021.

Vincent, R. A., Kovalam, S., Murphy, D. J., Reid, I. M., and Younger, J. P.: Trends and Variability in Vertical Winds in the Southern Hemisphere Summer Polar Mesosphere and Lower Thermosphere, Journal of Geophysical Research: Atmospheres, 124, 11 070–11 085, https://doi.org/https://doi.org/10.1029/2019JD030735, 2019.

Volz, R., Chau, J. L., Erickson, P. J., Vierinen, J. P., Urco, J. M., and Clahsen, M.: Four-dimensional mesospheric and lower thermospheric wind fields using Gaussian process regression on multistatic specular meteor radar observations, Atmospheric Measurement Techniques, 14, 7199–7219, https://doi.org/10.5194/amt-14-7199-2021, 2021.

Vondrak, T., Plane, J. M. C., Broadley, S., and Janches, D.: A chemical model of meteoric ablation, Atmospheric Chemistry and Physics, 8, 7015–7031, https://doi.org/10.5194/acp-8-7015-2008, 2008.

Walterscheid, R. L. and Hocking, W. K.: Stokes Diffusion by Atmospheric Internal Gravity Waves, Journal of Atmospheric Sciences, 48, 2213 – 2230, https://doi.org/10.1175/1520-0469(1991)048<2213:SDBAIG>2.0.CO;2, 1991.

Webster, A. R., Brown, P. G., Jones, J., Ellis, K. J., and Campbell-Brown, M.: Canadian Meteor Orbit Radar (CMOR), Atmospheric Chemistry and Physics, 4, 679–684, https://doi.org/10.5194/acp-4-679-2004, 2004.

Wilhelm, S., Stober, G., and Chau, J. L.: A comparison of 11-year mesospheric and lower thermospheric winds determined by meteor and MF radar at 69° N, Annales Geophysicae, 35, 893–906, https://doi.org/10.5194/angeo-35-893-2017, 2017.

Wilhelm, S., Stober, G., and Brown, P.: Climatologies and long-term changes in mesospheric wind and wave measurements based on radar observations at high and mid latitudes, Annales Geophysicae, 37, 851–875, https://doi.org/10.5194/angeo-37-851-2019, 2019.

Yuan, T., She, C. Y., Oberheide, J., and Krueger, D. A.: Vertical tidal wind climatology from full-diurnal-cycle temperature and Na density lidar observations at Ft. Collins, CO (41°N, 105°W), J. Geophys. Res. Atmos., 119, 4600–4615, https://doi.org/10.1002/2013JD020338, 2014.

Zängl, G., Reinert, D., Rípodas, P., and Baldauf, M.: The ICON (ICOsahedral Non-hydrostatic) modelling framework of DWD and MPI-M: Description of the non-hydrostatic dynamical core, Quarterly Journal of the Royal Meteorological Society, 141, 563–579, 2015.

Zhong, W., Xue, X., Yi, W., Reid, I. M., Chen, T., and Dou, X.: Error analyses of a multistatic meteor radar system to obtain a three-dimensional spatial-resolution distribution, Atmospheric Measurement Techniques, 14, 3973–3988, https://doi.org/10.5194/amt-14-3973-2021, 2021.

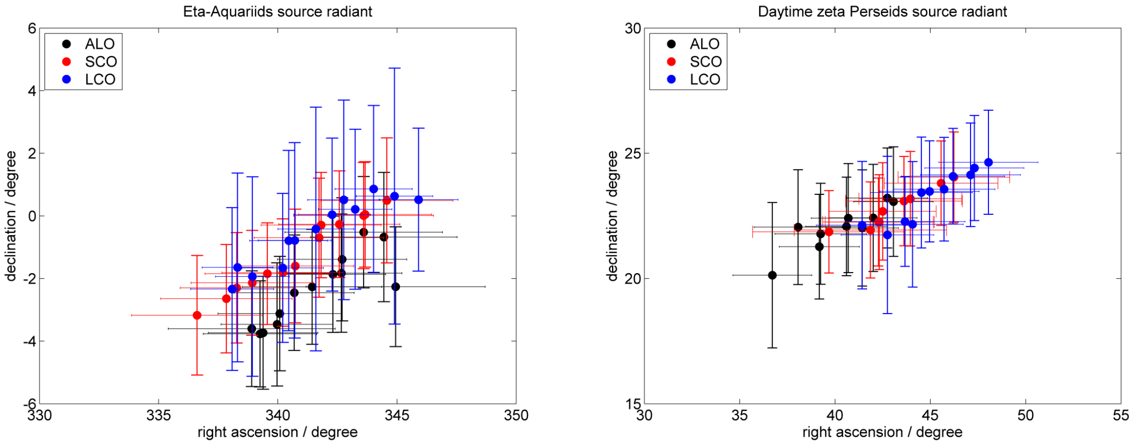

Figure B1. Scatter plots of meteor source radiant tracking for the Eta-Aquariids and Daytime Zeta-Perseids.